This manuscript has been published online in: Journal of the Mechanical Behavior of Biomedical Materials 2019 Dec

https://doi.org/10.1016/j.jmbbm.2019.103606

Title: Polymeric nanoparticles for endodontic therapy

Authors: Manuel Toledano[1], Estrella Osorio[a], Fátima S. Aguilera[1], Esther Muñoz-Soto[1], Manuel Toledano-Osorio[1,*], Modesto T. López-López[2], Antonio L. Medina-Castillo[3], Álvaro Carrasco-Carmona[1] and Raquel Osorio[1].

Institution:

[1] University of Granada, Faculty of Dentistry, Dental Materials Section. Colegio Máximo de Cartuja s/n, Granada 18071, Spain.

[2] University of Granada, Faculty of Science, Applied Physics Department. Fuente Nueva s/n, Granada 18071, Spain.

[3] NanoMyP, Spin-Off Enterprise from University of Granada. Edificio BIC-Granada, Avda. Innovación 1, Armilla, Granada 18016, Spain.

*Corresponding author: Manuel Toledano-Osorio

University of Granada, Faculty of Dentistry

Dental Materials Section

Colegio Máximo de Cartuja s/n

18071 – Granada - Spain.

Tel.: +34-958243789

Fax: +34-958240809

Email: mtoledano@correo.ugr.es

ABSTRACT

The effectiveness of novel polymeric nanoparticles (NPs) application in reducing dentin permeability and facilitating dentin remineralization after endodontic treatment was evaluated. The effect of undoped NPs, zinc, calcium and doxycycline-doped NPs (Zn-NPs, Ca-NPs and D-NPs, respectively) was tested in radicular dentin. A control group without NPs was included. Radicular dentin was assessed for fluid filtration. Dentin remineralization was analyzed by scanning and transmission electron microscopy, energy-dispersive analysis, AFM, Young´s modulus (*E*i), Nano DMA, Raman, and X-Ray Diffraction analysis. Ca-NPs and Zn-NPs treated dentin exhibited the lowest microleakage with hermetically sealed dentinal tubules and a zinc-based salt generation onto dentin. Zn-NPs favored crystallinity and promoted the highest *Ei* and functional remineralization at the apical dentin, generating differences between the values of complex modulus among groups. Ca-NPs produced closure of tubules and porosities at the expense of a relative mineral amorphization, without creating zones of stress concentration. The highest sealing efficacy was obtained in Zn-NPs-treated samples, along with the highest values of Young´s modulus and dentin mineralization. These high values of *Ei* were obtained by closing voids, cracks, pores and tubules, and by strengthening the root dentin. When using undoped NPs or Ca-NPs, deposition of minerals occurred, but radicular dentin was not mechanically reinforced. Therefore, application of Zn-NPs in endodontically treated teeth previous to the canal filling is encouraged.

Keywords: Endodontics; mineralization; NanoDMA; nanoparticles; Raman; sealing ability.

1. Introduction

Dentin is a highly mineralized hard tissue. Its mechanical properties are influenced by the type of mineralization, by the stress and strain tooth behavior. Extracellular matrix of dentin, in part, is formed by carbonate rich and calcium deficient hydroxyapatite (HAp) (Marshall et al., 1997), organized at intrafibrillar and extrafibrillar compartments of the collagen fibers. About 50% of the mineral volume in the dentin structure is composed of sub-micrometer to nanometer-sized, calcium deficient and carbonate rich apatite crystallites. Parallel, micrometer-sized, hypermineralized, collagen-poor hollow cylinders, and dentinal tubules, containing peritubular dentin, are dispersed between the dentin structure. The region localized between the tubules is occupied by intertubular dentin. Dentinal tubules converge to dental pulp (Kinney et al., 2003).

Dental caries is the localized dental hard tissue destruction. If the disease is not treated might eventually progress to cavitation (Fontana et al., 2010). If the appropriate treatment is not applied, the dental pulp is invaded by microorganisms through the exposed dentinal tubules. Hence, root canal treatment or endodontics can be required (Zheng et al., 2019). In root canal therapy, the main objectives are the pathological pulp removal, root canal system cleaning and shaping, contaminated root canals disinfection, and root canal system obturation in three dimensions in order to avoid reinfection (Torabinejad et al., 2005).

An endodontically-treated tooth is more likely to failure; this is due to the tooth structure damage caused by caries disease, access cavity preparation, and instrumentation of the canal. Within its properties, root dentin presents gradual spatial transition with regional variations from the cervical to the apical dentin, as a decrease of the mineral presence percentage is observed. Moreover, the inner wall is where the energy dispersion concentrates inside the root canal (Brosh et al., 2018). Therefore, the deformation and

stress concentration have defined the cervical radicular dentin as a potential failure site (Kaushik et al., 2018). However, during endodontics instrumentation procedures, a maximal tensile strength tends to appear at the root apical region (Brosh et al., 2018). As a clinical consequence, after endodontic treatment, the fracture strength of the apical root is drastically reduced (Patil et al., 2017).

The reinforcement of the root dentin, after endodontic treatment, has gained prominence in the last decade (Yoo et al., 2018). The use of endodontic sealers and cements destined to fill microcraks, cavities, pores and capillary channels is mandatory for a successful root canal therapy (Batool et al., 2018). Proposed materials range from the use of the glass-ionomer (Monticelli et al., 2007), silicate aluminum based cements (Torabinejad et al., 1993), to epoxy resins root canal sealers such as AH-Plus (Hakki et al., 2013), but most of them have shown different clinical shortcomings (Toledano et al., 2019c).

Controlled delivery of drugs is crucial for the clinical treatment trying to strengthen radicular dentin (Yoo et al., 2018). Nowadays, this can be achieved as a result of the rapid advances of nanotechnology, and due to the increased use of nanoparticles (NPs) (Chieruzzi et al., 2016; Negi et al., 2017). Novel polymeric NPs (100-nm in diameter) with anionic carboxylate (*i.e.*, COO^-) groups placed along the backbone of the polymer, that may be loaded with calcium (Ca-NPs), zinc (Zn-NPs) or doxycycline (D-NPs) are proposed to facilitate dentin remineralization of endodontically treated teeth. These NPs have previously been tested at the resin-dentin bonded interface (Osorio et al., 2016b; Toledano et al., 2017a). They are able to bind to the collagen and to facilitate the generation and precipitation of amorphous calcium-phosphate precursors (Toledano-Osorio et al., 2018b). Improved mineral maturation and remineralization have also been attained after NPs application on cervical dentin (Toledano et al., 2019a). Zinc and calcium serve as cofactors in several remineralization processes (Maret, 2013).

Doxycycline potentiates hard tissues regeneration in periodontal defects when locally administrated because of its anticollagenolytic effect (Agarwal et al., 2013). D-NPs may also reinforce the dentin microstructure, raising cracking resistance (Liss et al., 2003; Toledano et al., 2017a).

These NPs have been shown to exert an antimicrobial effect in previous *in vitro* studies (Toledano-Osorio et al., 2018a; Sánchez et al., 2019), reduce bacterial biofilm formation (Sánchez et al., 2019) and are nontoxic to fibroblasts (Osorio et al., 2016a). Some of the main targets of root canal treatment include the reinforcement of the cut dentin, the recovery of the dentin micro-structure and the reestablishment of the dentin chemical and mechanical properties (Toledano et al., 2018, 2017b). Hence, the objective of this research was to assess dentin permeability and remineralization after dentin infiltration with experimental NPs as a previous step to the endodontic sealer placement. The tested null hypothesis was that novel NPs application did not influence, at the short term or overtime, dentin micropermeability, neither remineralization of the endodontically treated radicular dentin.

2. Materials and Methods

2.1. Nanoparticles production

PolymP-*n* Active nanoparticles (NPs) (NanoMyP, Granada, Spain) were obtained through polymerization precipitation. In order to control the process of precipitation, a thermodynamic approach has been used: the Flory-Huggins model based on the Hansen solubility parameters. The model was developed basing on the growing polymeric chains and solvent molecules interactions by hydrogen-bonding, polar and dispersion forces (Medina-Castillo et al., 2010). The NPs are designed with 2-hydroxyethyl methacrylate as the backbone monomer, the methacrylic acid as the functional monomer and ethylene

glycol dimethacrylate as the cross-linker. NPs doped with calcium (Ca-NPs) and zinc (Zn-NPs) were produced. The NPs complexation processes with zinc and calcium were realized via immersion of 30 mg of NPs in aqueous solutions of 15 mL of $ZnCl_2$ or $CaCl_2$ (containing zinc or calcium at 40 ppm at pH 6.5) for 3 days at room temperature under constant shaking, with the objective of reaching the metal ions adsorption equilibrium (Osorio et al., 2016b). The suspensions were subsequently centrifuged (7800 rpm/G-force=6461) for 20 min and the particles were detached from the supernatant. The same centrifugation technique, with the addition of phosphate buffer solution (PBS) to wash the sample, was repeated twice. Achieved values of ion complexation were 0.96 ± 0.04 μg Ca/mg NPs and 2.15 ± 0.05 μg Zn/mg NPs (Osorio et al., 2016a). 30 mg of NPs were immersed in 18 mL of 40 mg/mL doxycycline hyclate aqueous solution (Sigma Aldrich, Chemie Gmbh, Riedstr, Germany) for 4 hours, under constant shaking. 933 μg Doxycycline per mL (Dox/mL) were loaded for every NPs mg (Toledano-Osorio et al., 2018a). The NPs distributions of the hydrodynamic size, assessed by dynamic light scattering in deionized water, are: NPs 250.10 nm, D-NPs 244.36 nm, Zn-NPs 225.93 nm and Ca-NPs 238.10 nm. After loading, the size of NPs is not altered, and there is not production of NPs agglomeration (Toledano-Osorio et al., 2018b). NPs suspension in ethanol was obtained at 10 mg/mL concentration: 1) undoped NPs (NPs), 2) doxycycline hyclate-doped NPs (D-NPs), 3) Ca-doped NPs (Ca-NPs), and 4) Zn-doped NPs (Zn-NPs).

2.2. Teeth specimen preparation and nanoparticles application

Eighty human mandibular premolars were obtained from donors (18-25 yr of age) with single roots and vital pulp, extracted for periodontal or orthodontic reasons and without caries lesions. The informed consent for inclusion was obtained from all subjects before their participation in the study. The procedure was undertaken following the Declaration

of Helsinki, and the approval of the protocol was carried out by the Institution Review Board (#405/CEIH/2017). A random selection procedure was realized to select the teeth samples and they were conserved at 4 °C in 0.5% chloramine T bacteriostatic/bactericidal solution for up to 1 month. The storage medium had to be replaced every week. The decoronation of the teeth was realized with a low-speed diamond saw (Accutom-50 Struers, Copenhagen, Denmark), and the length of the root was standardized to approximately 12 mm and radiographed at 2 angulations to check the presence of a single canals. The treatment of the root canal began with the use of Gates Glidden drills (Dentsply Maillefer, Ballaigues, Switzerland), size 2 and 3, to shape the roots coronal third part. Subsequently, a size 15 Flex-o-file (Dentsply Maillefer, Ballaigues, Switzerland) was used to achieve a canal patency. The working length was recorded, and it was established 0.5 mm shorter than apical foramen. ProTaper nickel-titanium rotary instruments (Dentsply Maillefer, Ballaigues, Switzerland) up to size F4 were used for the final instrumentation. During the instrumentation procedures, the root canal was irrigated by means of a 27-gauge needle with 0.5 mL of 5% sodium hypochlorite (NaOCl, Panreac, ref. n. 212297), while at the end of canal instrumentation 0.5 mL of a 17% EDTA solution were used for 3 min (MD-Cleanser, Meta Biomed, Chungbuk, Republic of Korea) to remove the smear layer (O'Connell et al. 2000). Each specimen was finally irrigated with 0.5 mL of 5% NaOCl for 1 min, followed with distilled water for one more minute, and dried with paper points (Dentsply Maillefer). The following steps of the endodontic treatment were realized as in Toledano et al. (2019c). The specimens were randomly separated in 5 groups (n = 16); 100 µl of the four different NPs suspensions at 10 mg/mL were introduced into the teeth roots using a sterile micropipette. In one of groups, NPs were not applied (control group). Afterwards, in all groups, AH-Plus sealant cement (Dentsply Maillefer, Ballaigues, Switzerland) was applied and one size 30 guttapercha

(guttacore) cone (Dentsply Maillefer, Ballaigues, Switzerland) was placed and compacted into the canal to working length. The adequate obturation of the material along the root canal and the voids absence was evaluated with two angulations that were realized to assess radiographically each tooth (Mestres et al., 2014; Monticelli et al., 2010; Vizgirda et al., 2004).

2.3. Sealing ability trough the fluid filtration system

After storing the filled root canals in simulated body fluid solution [SBFS: NaCl, $NaHCO_3$, KCl, K_2HPO_4, $MgCl_2$, $CaCl_2$, and $(CH_2OH)_3$ CNH_2/HCl (6 N) to buffer the pH (7.4)], 10 teeth from each group (n=50) were coated with two layers of varnish up to 2 mm from the root apex (Bouillaguet et al., 2008). The coronal part was bound to a plexiglass support with cyanoacrylate adhesive (Rocket, Corona, CA, USA). A 18-gauge needle penetrated 2 mm into the root coronal piece through the Plexiglas support. The other end of the 18-gauge needle was inserted into an 18-gauge polyethylene tubing (R-3603, Tygon, Paris, France) to assess the filled roots microfiltration. A liquid flow sensor (ASL 1600, Sensirion, Staefa, Switzerland) connected between the root specimen and the source of hydraulic pressure was employed to quantify the filled root canals fluid flow. A syringe suspended 70 cm above the sensor and filled with 60 mL of deionized water generated a constant hydraulic pressure of 6.86 kPa. The specimens were stored in SBFS and the medium was refreshed every 2 weeks. The rest of the fluid flow method of the filled root canals was assessed as in Toledano et al. (2019b) at different storage times (24 hours, 1 week, 3 months and 6 months) (Scheme 1A).

SCHEME 1

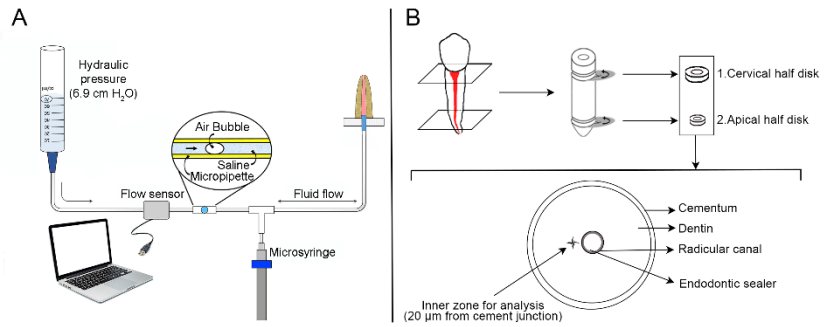

Scheme 1. A, Schematic illustration showing dentin permeability measurement. Samples were connected to a hydraulic pressure device under a constant hydraulic pressure. The dimensions of the changes in fluid volume were attained via a digital sensor. **B**, Schematic representation of the specimen preparation for interfacial assessment. Tooth coronal section was eliminated. Two disks of cervical and apical root dentin were obtained. Inner dentin zones were measured.

2.4. Nanoindentation and AFM analysis

Thirty teeth were employed for this part of the study. Half of the specimens were studied at 24 h of storage, while the other half was studied after 6 months. To isolate regions in the cervical and apical root dentin, two radicular disks were obtained from each root (13.5 and 4.5 mm respectively, above apex), by splitting perpendicularly to their long axis into 1 mm ($\pm$0.1 mm) thick slices (Scheme 1B). The crowns were discarded at the cement-enamel junction, using a water-cooled diamond saw (Accutom-50 Struers, Copenhagen, Denmark). Two samples slabs with a 1 mm thickness were obtained sectioning bucco-lingually the root canal to examine cervical and apical areas (Scheme 1B). 800 up to 4000 grit SiC abrasive papers were used to polish the surfaces. The final polishing steps were done by using diamond pastes through 1 µm down to 0.25 µm (Struers LaboPol-4; Struers GmbH, Hannover, Germany) (Scheme 1B). After each polishing step, samples were treated with deionized water for 5 min in ultrasonic bath (Model QS3, Ultrawave Ltd, Cardiff, UK).

2.4.1. Young's modulus and Nano-DMA analysis

In this study, a Hysitron Ti-750D TriboIndenter indentation system (Hysitron Inc., Minneapolis, MN) equipped with a commercial nano-DMA package was employed. A Berkovich (three sides pyramidal) diamond tip (tip radius ~20 nm) was used as the nanoindenter. The calibration of the nanoindenter tip was performed over a fused quartz sample. A quasistatic force setpoint of 5 μN was used. The calibration-reduced modulus value of 1.1400E+03 N/mm^2 was employed to obtain the best-fit spherical radius (150 nm). Ten dentin indentations were performed on each specimen at 20 μm next to radicular canal (inner zone) (Scheme 1B). A load of 4000 nN and a time function of 10 s were used to execute the indentations. The tip pressed progressively over the sample (at a constant rate) up to a peak load of 4000 μN. The indentations were performed in a hydrated condition (Toledano et al., 2019b; Toledano-Osorio et al., 2018b).

Dentin disks were also subjected to nano-DMA analyses. A dynamic (oscillatory) force of 2 μN was superimposed on the quasistatic signal at a frequency of 200 Hz. Based on a calibration-reduced modulus value of 69.6 GPa for the fused quartz, the best-fit spherical radius approximation for tip was found to be 150 nm, for the selected nano-DMA scanning parameters. Modulus mapping was conducted by imposing a quasistatic force setpoint, Fq=2 μN, to which it was superimposed a sinusoidal force of amplitude FA=0.10 μN and frequency f=100 Hz. The resulting displacement (deformation) at the site of indentation was monitored as a function of time. Data from regions, approximately 50×50 μm in size, were collected using a scanning frequency of 0.2 Hz. Both Young' s modulus (Ei) and complex modulus (E*) were calculated.

2.4.2. Atomic Force Microscopy (AFM), nanoroughness and fibrils width assessments

Topography mappings were obtained with an atomic force microscope (AFM Nanoscope V, Digital Instruments, Veeco Metrology group, Santa Barbara, CA, USA). The images

were obtained, in a fully hydrated state, inside a fluids cell of the AFM using the tapping mode with a calibrated vertical-engaged piezo-scanner (Digital Instrument, Santa Barbara, CA, USA). An oscillating cantilever with a 10 nm radius silicon nitride tip (Veeco) contacted intermittently with the dentin surface at the lowest point of the oscillation. Changes in vertical position of the AFM tip at resonance frequencies near 330 kHz provided the height of the images registered as bright and dark regions. 15 x 15 μm digital images were recorded with a slow scan rate (0.1 Hz). For each image, 5 randomized boxes (2 x 2 μm) were created to examine the nanoroughness at 24 h and 6 m of storage. Nanoroughness (SRa, in nanometers) was measured with proprietary software (Nanoscope Software, version V7). Collagen fibril diameter was determined from 2 x 2 μm images by section analysis using data that had been modified only by plane fitting. The collagen fibril diameter was preferentially determined from fibrils that were exposed along their complete widths. Five fibrils were analyzed from each image (Toledano et al. (2019a). Measurements were corrected for tip broadening (Habelitz et al., 2002) by the equation $e=2r$, where e is the error in the horizontal dimension and r is the tip's radius (Takeyasu et al., 1996).

2.5. Statistical Analysis

Microleakage, nanoindentation, Young's modulus, complex modulus, fiber diameter and nanoroughness were statistically analyzed. The normality and homoscedasticity conventions of the data were valid. Microleakage, nanoindentation, Young's modulus, complex modulus, fiber diameter and nanoroughness were considered dependent variables in each ANOVA model. NPs, storage time and dentin zone were independent influencing factors. Interactions between pairs of factors (always including NPs type) were analyzed. If interactions were significant, groups of NPs were not pooled and

compared by *Student-Newman-Keuls* multiple comparisons test or *Student t test*. Statistical significance preset at $p<0.05$.

2.6. Raman spectroscopy

Dentin surfaces were subsequently studied with Raman spectroscopy. For this analysis, it was employed a dispersive Raman spectrometer/microscope (Horiba Scientific Xplora, Villeneuve d´Ascq, France) with a 785-nm diode laser through a X100/0.90 NA air objective and with 500 μm pinhole. The spectrometer was equipped with a CCD detector (DR-324B-FI-327, Andor Technology LTD, UK). The 785 nm laser was used with 100X objective. A 600-lines/mm gratting centered between 400 and 1700 cm^{-1} was used to obtain Raman signals. The surfaces were submitted to a chemical mapping. Two surface areas of 12x12 μm were mapped at dissimilar sites for each sample at X and Y axis with a 0.5 μm spacing (625 points per map) and each spectrum was measured by using 2s acquisition time with 2 accumulations. Baseline correction was always performed after acquisition in order to subtract background; a 5^{th} degree polynomial function was used for that purpose. Chemical mapping was submitted to K-means cluster (KMC) analysis using the multivariate analysis tool (ISys® Horiba), which includes statistical pattern to derive the independent clusters. The K-means clustering is a method of analysis based on a centroid model which aims to partition "n" observations into "k" clusters in which each observation belongs to the cluster with the nearest mean. The natural groups of components (or data) based on some similarity and the centroids of a group of data sets were found by the clustering algorithm once calculated by the software and the Hierarchical Cluster Analysis (HCA). The observed spectra were described at 400-1700 cm^{-1} with 10 complete overlapping Gaussian lines, suggesting homogeneous data for further calculations (Ager et al., 2005). Each cluster biochemical content was examined

though the average cluster spectra. Using the Hierarchical Cluster Analysis (HCA) and the algorithm calculated by the software, the natural groups of components (or data) based on some similarity and the centroids of a group of data sets were found. At this point, the dentin mineral component was assessed studying the relative presence of mineral, *i.e*, phosphate (960 cm^{-1}) peak and area, and the relative mineral concentration of phosphate (PO_4^{3-}) referred to phenyl (RMC_p). The dentin organic component was analyzed examining the crosslinking at 1030-1032.7cm^{-1} (pyridinium ring vibration). The ratio amide III/AGEs pentosidine, for nature of collagen, and the 1340 cm^{-1} peak, indicative of organization, altered quality, differences in the structure, and orientation of α-helices at collagen (Salehi et al., 2013; Wang et al., 2009), were also assessed.

2.7. X-Ray Diffraction (XRD) analysis

Disks were then cut into two halves. One half of each specimen was yielded to XRD analysis. Surfaces were polished using 600, 1200, 2400 and 4000 grit SiC abrasive papers on a water-cooled polishing device (Buehler-MetaDi, Buehler Ltd. Lake Bluff, IL, USA). A final ultrasonic cleaning (10 min) concluded the specimen preparation. In this experiment, the X-ray micro-diffractometer (μXRD^2) was a single crystal diffractometer Bruker-D8 Venture (Bruker AXS, Germany) equipped with a 2-dimensional detector system CMOS Photon 100 (Bruker AXS, Germany), and a kappa geometry-based goniometer 2D Detector. The X-Ray beam (Cu Kα line, λ = 1.5418 Å) was generated by a Cu microforms source IμS and generator settings of 50 kV/1 mA were employed. The 2D position sensitive detector had 1024x1024 pixels. The beam collimator length was 90 mm and its diameter 0.1 mm (spot size 100 μm). The crystal to detector distance was calibrated with a sample of ylid. The sample was mounted on the XYZ goniometer with the surface to be analyzed placed normal to the φ axis. Then the goniometer was

automatically adjusted to bring the sample surface into focus, with the region of interest in the center of the crosshair of the video window by means of a video camera system (NTSC-Digital Video Camera. Model LCL-211H, Watec America Corp.,USA). The considered kappa goniometer positions at 40 mm distance were: 2θ, 40º; ω, 20º; φ, 270º; χ, 50º. All measurements were performed at room temperature (295±0.1°K) and an exposure time of 60 s. Three images were obtained from each of the six specimens produced for each experimental group, a total of 18 frames were recorded. The final refined μXRD^2 profile and Debye-Scherrer rings image (pole image) of each group were obtained by accumulating all X-ray energies (wavelengths) in a single image. The results are commonly presented as maximum positions in 2θ (x) and X-ray counts (intensity) (y) in the form of an x-y chart. The XRD2DScan software (Rodríguez-Navarro, 2007) was employed, as it allows all images to be integrated into a representative single image. The whole batch of the measured frames was loaded and all frames were processed; then a single file was created. This file contains the variation of intensity along the Debye ring associated with the selected reflection as a function of angle, for every processed frame. All this information was used to construct the final refined μXRD^2 profile and pole image. The crystallites size and preferred orientation were calculated from the X-ray micro-diffraction pattern (Perales et al., 2008; Xue et al., 2013):

$$d = \frac{K\lambda}{\beta \cos\theta}, \quad (1)$$

In this equation d is the mean size of the crystallites, K is a dimensionless shape factor, with a value close to unity –note that in the case of dentin, $K \approx 0.94$ (Xue et al., 2013), and β is the peak full width at half maximum (FWHM) of the line broadening. In order to assess the crystallite width and length, this equation was employed for the line broadenings corresponding to 002 (H) and 310 (L) reflections, respectively. The texture,

crystallites preferred orientation, was obtained from the following intensity ratios (Xue et al., 2013):

$$R_{hkl} = k_{hkl}\frac{I_{211}}{I_{hkl}}, \quad (2)$$

In this formula, I_{211} and I_{hkl} correspond respectively to the intensities of the line reflections 211 and *hkl*, and

$$k_{hkl} = \frac{I_{hkl}^{st}}{I_{211}^{st}}, \quad (3)$$

where the superscript *st* refers to intensities calculated according to the JCPDS card (Low, 2004; Xue et al., 2013).

2.8. Field Emission Scanning Electron Microscopy (FESEM), energy dispersive (FESEM/EDX) and Transmission Electron Microscopy (TEM) analyses

The second half of each specimen was fixed for 24 h in a 2.5% glutaraldehyde solution in 0.1 mol/L sodium cacodylate buffer. To observe the samples with a field emission scanning electron microscope (FESEM Gemini, Carl Zeiss, Oberkochen, Germany), they were exposed to critical point drying (Leica EM CPD 300, Wien, Austria) and sputter-coated with carbon by means of a sputter-coating Nanotech Polaron-SEMPREP2 (Polaron Equipment Ltd., Watford, UK). An X-ray detector system (EDX Inca 300, Oxford Instruments, Oxford, UK) attached to the FESEM realized an energy-dispersive analysis in designated points. After XRD analysis, same samples were submitted to TEM analysis. Each half disk (1mm thickness) was transversally sectioned at three points: 1) in the middle, 2) at both sides right and left about 500 microns from the interface. Specimens were then ground from the external surface (cementum) until a 100 µm distance from the sealer-dentin interface. Grinding was performed by using 600, 1200 and 2400 grit SiC abrasive papers on a water-cooled polishing device (Buehler-MetaDi, Buehler Ltd. Lake Bluff, IL, USA). A final ultrasonic cleaning (10 min) concluded the

specimen preparation. Samples were crushed into a fine-grained powder in a liquid nitrogen mortar and pestle, and 2% NaOCl was added to remove the surrounding collagen, with daily changes for a week (using a sonicator). After washing with H_2O and ethanol, the nanocrystals were transferred to a 3 mm diameter carbon/Formvar coated cooper TEM grid. Before analysis, all samples were sputter coated with a thin layer of amorphous carbon. Electron lucent particles were selected by size and distant from grid bars. The samples were analyzed using a Transmission Electron Microscope Zeiss Libra 120 (Oberkochen, Germany) at 120 kV in bright-field (BF), and selected area electron diffraction (SAED) patterns were also captured. Normal BF images were produced by tilting the beam to the diffracting plane of interest. Tomographic reconstructions and related data were processed with the software iTEM (Olympus Soft Imaging Solutions GmbH, Münster, Germany), comprising acquisition, alignment and visualization. A specific semi-automated modulus for image processing, attached to the microscope, including a 2048x2048 pixel chip BM-2k-120 Dual-Speed on axis SSCCD-camera (TRS, Moorenweis, Germany), was used. The obtained images were aligned and back projected using the software for 3D from the iTEM tomography extension. Reconstructions were achieved with a silicon graphics workstation self-incorporated. Nanoindentation, AFM, Raman, FESEM, EDX and TEM analyses were executed at 24 h and 6 m after SBFS storing.

3. Results

3.1. Sealing ability trough the fluid filtration system

The fluid filtration rate ($\mu L\ min^{-1}$) at distinct storage time for all groups is shown in Figure 1. Significant differences ($P<0.05$) were found between groups. Zn-NPs promoted the lowest microleakage values, at 24 h time point. After 6 m of storage, samples treated with

undoped NPs, Ca-NPs and Zn-NPs, showed the lowest microleakage scores (P<0.05). D-NPs and control groups attained the highest microleakage values. Samples treated with D-NPs did not modify their microleakage outcomes over time, except at 3 m time point, which decreased (P<0.05). In general, when Zn-NPs were used, microleakage was similar over time.

FIGURE 1

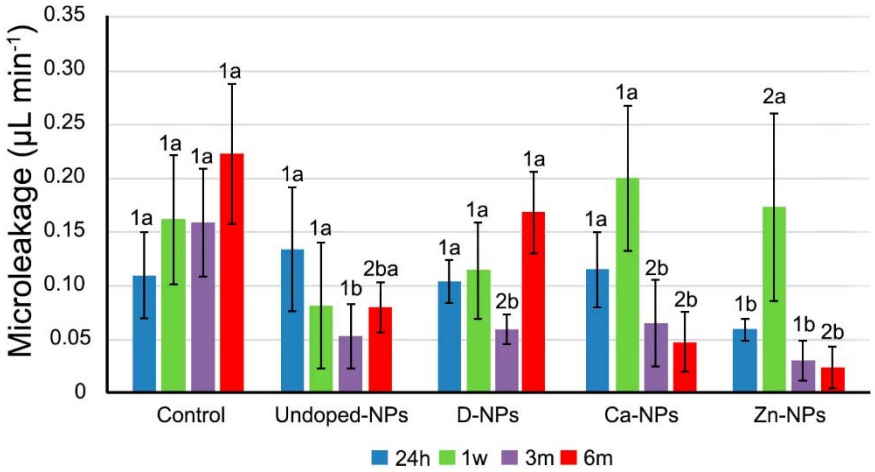

Figure 1. Microleakage values (mean and SD) obtained for each experimental group. Identical lower case letter indicate no significant differences between time points at each NPs group. Same numbers indicate no significant differences among NPs within the same time point ($p < 0.05$).

3.2. Nanoindentation

Mean and SD of the modulus of Young (*Ei*) at the two different dentin disks (cervical and apical) are represented in Table 1. Specimens treated with Zn-NPs attained the highest *Ei* at both cervical and apical dentin, among groups, at 6 m of storage. Specimens treated with Zn-NPs raised their Young's modulus, after storage, at both cervical and apical peritubular dentin. At peritubular cervical dentin, specimens treated with Ca-NPs attained the lowest modulus of Young at 6 m of storage (Table 1).

After 6 m of storage, apical dentin treated with both unloaded NPs and Ca-NPs achieved the highest complex modulus (E^*), among groups (Table 1). Control samples and those treated with Zn-NPs (Figure S1A) showed the lowest E^* at apical root dentin.

Table 1. Mean and standard deviation (SD) values of Young's modulus (GPa) and complex modulus (GPa) attained at the different experimental groups.

	Young's modulus (*Ei*)								**Complex modulus (*E**) (GPa)**			
	Cervical Dentin				**Apical Dentin**				**Cervical Dentin**		**Apical Dentin**	
	Intertubular Dentin		**Peritubular Dentin**		**Intertubular Dentin**		**Peritubular Dentin**					
	24h	**6m**	**24h**	**6m**	**24h**	**6m**	**24h**	**6m**	**24 h**	**6m**	**24h**	**6m**
Control	23.01 (0.66) A1*	14.68 (2.64) a1	25.90 (4.23) A1*	16.42 (2.56) a1	22.19 (1.10) A1	24.82 (4.76) a2	24.43 (3.48) A1*	17.84 (2.49) a1	94.20 (11.20) 1Aa*	130.78 (21.60) 1Aa	25.80 (6.29) 2Ab	20.85 (15.63) 2Ab
NPs	23.81 (2.73) A1	20.78 (0.93) b1	21.50 (0.51) A1*	16.09 (2.88) a1	35.12 (3.23) B2	38.02 (4.27) b2	33.68 (2.82) B2	29.08 (2.76) b2	119.49 (15.47) 1Aa*	197.23 (19.30) 1Ba	107.37 (25.02) 1Ba*	171.85 (30.81) 1Ba
D-NPs	22.17 (0.49) A1*	15.88 (2.71) a1	25.46 (4.93) A1*	16.56 (1.22) a1	33.47 (2.69) B2	29.41 (7.29) ab2	32.82 (2.73) B2	29.80 (4.54) b2	53.71 (16.64) 1Ba	50.81 (11.68) 1Ca	59.72 (11.70) 1Ca	59.90 (8.63) 1Ca
Ca-NPs	15.57 (0.88) B1*	12.29 (2.49) a1	20.22 (3.51) A1*	12.12 (1.24) b1	23.17 (2.71) A2	22.71 (2.10) a2	27.33 (4.89) AB1*	16.55 (3.71) a1	67.26 (26.21) 1Ba*	166.90 (14.01) 1Aa	46.28 (6.72) 1Ca*	153.55 (18.31) 1Ba
Zn-NPs	22.86 (1.69) A1	27.15 (5.18) c1	21.89 (3.09) A1*	31.41 (5.74) c1	36.23 (3.30) B2*	41.35 (1.37) b2	33.25 (4.49) B2*	46.48 (4.45) c2	143.34 (16.98) 1Ca	152.87 (16.16) 1Aa	31.04 (3.25) 2Ab	42.77 (7.41) 2ACb

Abbreviations: NPs: Undoped/unloaded nanoparticles; D-NPs; Doxycycline doped nanoparticles; Ca-NPs: Calcium doped nanoparticles; Zn-NPs: Zinc doped nanoparticles. Young's modulus and Complex modulus were analyzed separately.

Young's modulus: Identical capital letter means no significant difference among distinct NPs at the same dentin half (cervical and apical) and zone (intertubular and peritubular) at 24 h. Identical lowercase indicates no significant difference between different NPs at the same dentin half (cervical and apical) and zone (Intertubular and Peritubular) at 6 m. Identical number indicates no significant difference between different dentin halves (cervical vs apical) within the same NPs at the same storage time (24 h and 6 m) and zone (intertubular and peritubular). Asterisks indicate significant difference between different storage time (24 h *vs* 6 m) within the same NPs at the same dentin half (cervical and apical) and zone (intertubular and peritubular).

Complex modulus: Data concerning the complex modulus were written in italic. Identical capital letter means no significant difference among distinct NPs at the same dentin half (cervical and apical) and storage period (24 h and 6 m). Identical lowercase means no significant difference among different dentin halves (cervical and apical) at the same NPs group and storage period (24 h and 6 m). Asterisks means significant difference between distinct storage time (24 h *vs* 6 m) with the same NPs at the same dentin half (cervical and apical).

3.3. Atomic Force Microscopy (AFM), nanoroughness and fibrils width assessments

Specimens treated with undoped NPs, Ca-NPs and Zn-NPs attained, in general, the highest fibrils width, and the controls and D-NPs the lowest, at both cervical and apical dentin after 6 m storage. Fiber diameter increased over time when cervical and apical dentin were treated with unloaded NP, Ca-NPs and Zn-NPs (Table S1). At 6 m storage, the highest nano-roughness values were attained by dentin samples treated with unloaded NPs. Zn-NPs treatment produced the lowest SRa values (Table S1) (Figure 2).

FIGURE 2

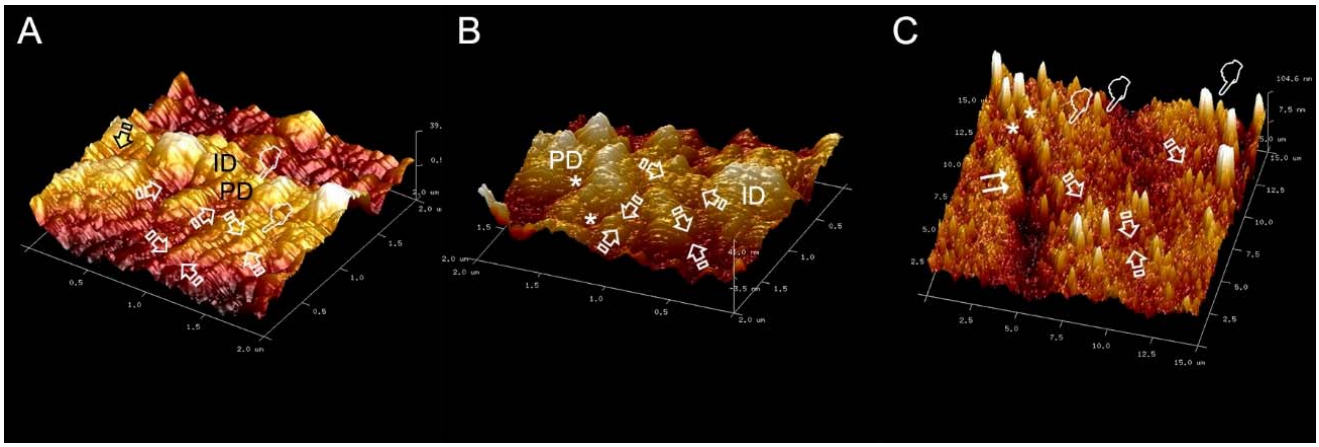

Figure 2. (**A**) 2 x 2 μm topographic mapping obtained by AFM at the inner zone of the apical dentin treated with Ca-NPs, after 6 m of storage. Peritubular (PD) and intertubular (ID) dentin mineralization is evidenced. Collagen fibrils, the bandwidth of the collagen fibrils and the wider bandwidth (faced arrows) with the staggered pattern of collagen fibrils are shown (pointers). (**B**) 2 x 2 μm topographic mapping obtained by AFM at the inner zone of the apical dentin treated with Zn-NPs, after 6 m of storage. Tubules were completely occluded (asterisks). Wider bandwidth of the collagen fibrils and the staggered pattern of collagen fibrils are shown (faced arrows). (**C**) 15 x 15 μm topographic mapping obtained by AFM at the inner zone of the cervical dentin treated with Zn-NPs, after 6 m of storage. Peritubular dentin appeared strongly remineralized (double arrows). Stick-slip images in radial direction of nucleated minerals resulted observable at the intertubular dentin, as sight of energy dissipation (pointers) The crack deflection and branching around the peritubular cuff, may be observed at the dentin wall of an unfilled tubule (single arrows). Strong processes of intertubular and intratubular mineralization, with protruding rounded forms were also observed (arrow head). Some bridge and rod-like new mineral formations were observed surrounding the intratubular crystals (asterisks). These crystals precipitated beams held the intratubular deposits of mineral to the peritubular dentin.

3.4. Raman spectroscopy

Ca-NPs-treated samples at the cervical root dentin achieved the highest phosphate peak (961 cm^{-1}) intensity among groups at 6 m (Table 2) (Figure 3A). Zn-NPs-treated specimens at the apical root dentin attained the highest intensity of phosphate peak, *i.e*, higher mineralization among groups at 6 m (Table 2) (Figure 3B). HCA Raman images (clusters) (Figures S3A and S3B) and results (centroids) (Figures S3C and S3D) achieved at Zn-NPs-treated specimens cervical dentin surface after 6 m of storage showed higher phosphate peaks and different variances, both corresponding to the three distinguishable centroids (HCA_1, HCA_2 and HCA_3), in comparison with the Ca-NPs-treated samples. After 6 m storage, mineralization measured trough the intensity of the phosphate peak at the cervical and apical dentin, was higher in samples treated with Zn-NPs and Ca-NPs if compared with the other groups of NPs (Table 2). Ca-NPs and Zn-NPs treated dentin showed the highest crosslinking (1032 cm^{-1}) of collagen, at cervical and apical dentin (Table 2).

Table 2. Raman intensities and ratios of mineral and organics components attained from dentin at the different experimental groups.

		MINERALS						ORGANICS					
		Relative Presence of Mineral Phosphate [960 cm^{-1}]						Crosslinking		Nature of collagen		Complementary index	
		Peak		Area		RMC (960/1001)		Pyridinium [1032 cm^{-1}]		Ratio AIII/AGEs		α-helices [1340 cm^{-1}]	
		24h	**6m**	**24h**	**6m**	**24h**	**6m**	**24h**	**6m**	**24h**	**6m**	**24h**	**6m**
Control	Cervical	518.10	360.27	15315	9061	17.14	25.15	34.36	16.65	0.01	0.23	9.86	8.81
	Apical	807.65	589.95	20507	14757	22.45	12.78	32.83	31.04	0.10	0.05	22.00	11.25
NPs	Cervical	470.47	568.70	13792	14036	11.88	17.15	28.58	25.56	0.05	0.09	9.52	6.15
	Apical	772.35	739.43	19133	18344	21.97	30.12	41.77	37.14	0.04	0.45	15.12	14.91
D-NPs	Cervical	542.79	446.13	13422	13052	13.96	23.35	30.97	22.72	0.02	0.26	4.06	11.53
	Apical	645.20	620.34	16174	15492	21.59	24.46	29.89	32.82	0.01	0.68	11.92	17.29
Ca-NPs	Cervical	372.92	735.10	10906	19131	7.72	27.67	25.70	40.17	0.12	0.19	8.63	17.38
	Apical	551.71	773.29	14324	19733	27.52	28.48	28.69	34.78	0.31	0.09	13.20	13.30
Zn-NPs	Cervical	542.30	621.82	14042	16086	7.69	23.70	36.49	37.39	0.16	0.09	7.65	8.96
	Apical	802.77	800.14	20229	20079	29.98	19.37	43.73	38.89	0.22	0.17	13.84	15.44

Abbreviations: NPs: undoped/unloaded nanoparticles; D: Doxycycline; Ca: Calcium; Zn: Zinc; Mineral/Matrix (CH_2) Ratio; RMC: Relative mineral concentration between mineral/Phenyl (1003); AIII: Amide III (1690 cm^{-1}); AGEs: Advanced glycation end products (1550 cm^{-1}). For all the components, the peaks values had been normalized to the intensity of the Amide II band basis near 1510 cm^{-1}. Peaks positions are expressed in cm^{-1}.

FIGURE 3

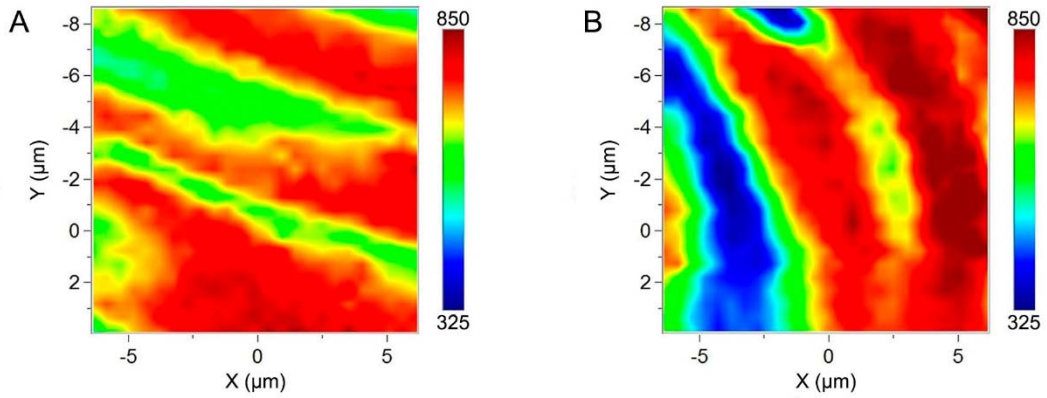

Figure 3. 2D micro-Raman map of the phosphate peak (961 cm^{-1}) intensities at samples treated with Ca-NPs (**A**) and Zn-NPs (**B**) at the cervical and apical radicular dentin, respectively, after 6 m of storage.

3.5. X-Ray Diffraction (XRD) analysis

The analysis of µXRD[2] profiles of root dentin indicated that the physical broadening (FWHM) of peaks at 002 (2θ, 25.900º; centroid peak position θ_{hkl}, 0/0/-2; I, 10977386) reflection, after observing data plotted by the reduced full width and extended height at half maximum of the phosphate band, achieved the highest values (more amorphous) at cervical dentin surfaces treated with undoped NPs (Table S2). After 6 m, peaks at 310 (2θ, 40.127º; centroid peak position θ_{hkl}, -3/1/0; I, 1380390) showed the lowest FWHM at cervical dentin treated with Zn-NPs and at apical dentin treated with Ca-NPs, denoting a crystalline status. At both 002 and 310 reflexions FWHM decreased over time, gaining in crystallinity (Table S2). When dentin was treated with Zn-NPs at 6 m of storage, the reflection at 002 peak and the diffraction rings corresponding to 002 plane (Figures 4A, 4B and S4E), showed higher crystallinity values than those obtained in the rest of the groups (Figures S4A, S4B, S4C and S4D).

FIGURE 4

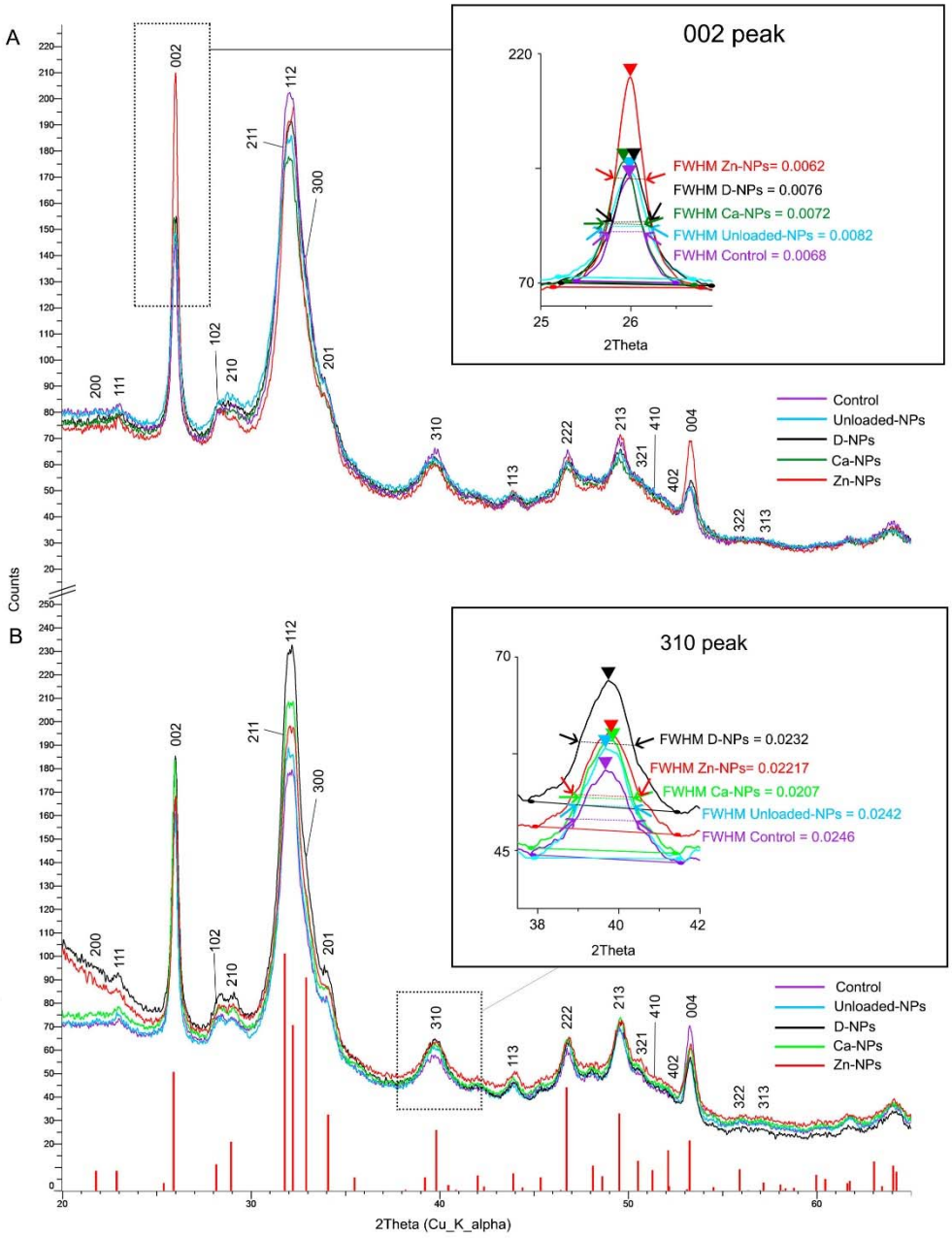

Figure 4. Refined μXRD^2 profiles of cervical (**A**) and apical (**B**) root dentin after 6 m of storage. Insets (**A** and **B**) represent two truncated μXRD^2 profiles after observing the reflection at 002 and 310 peaks, respectively, and further full width half maximum (FWHM) measurements. Vertical bars represent HAp peaks.

A qualitative estimation of the size of the coherently scattering domain (*i.e.* the crystallite size) is reported in Table S2. The longest crystallite size was obtained after using Zn-NPs at the root dentin apical section [τ_{002} (*H*)] (24.16 nm). The highest value of grain size appeared after treating the cervical dentin with Zn-NPs (23.55 nm). At 310 reflexions, the

highest and lowest grain size corresponded to Zn-NPs and Ca-NPs-treated samples, respectively (Table S2). The lattice strain within the long dimension (002 reflection) was also higher in case of treating cervical dentin with Zn-NPs ($9.7x10^{-7}$), at 6 m. At 310 reflexions, Zn-NPs achieved the lowest lattice strain at cervical dentin ($1.2x10^{-5}$) (Table S2). At 002 plane and at 6 m storage, the texture measured at all sealers-treated cervical dentin followed the trend: control > undoped NPs > D-NPs > Ca-NPs > Zn-NPs. At the apical section of dentin, the trend in texture was: D-NPs > Zn-NPs > undoped NPs > Ca-NPs > Control. At 310 plane, the cervical dentin performed in texture as follows: Zn-NPs > Control > D-NPs > undoped NPs > Ca-NPs. At the apical dentin the trend in texture was as follows: D-NPs > Ca-NPs > Zn-NPs > Control > undoped NPs (Table S2).

3.6. Field Emission Scanning Electron Microscopy (FESEM), energy dispersive (FESEM/EDX) and Transmission Electron Microscopy (TEM) analyses

After 6 m of storage and FESEM/EDX analysis, specimens treated with both Ca-NPs and Zn-NPs showed a generalized mineralization of intertubular dentin (Figures 5A·I and 5B·I), with evident calcium-phosphate salts deposits formation (Figure 5A·II and 5B·II), that totally occluded the dentinal tubules. Zn-NPs produced hermetically sealed tubules and peritubular dentin turned up strongly mineralized (Figure 5B·I). Gaps were showed at the canal sealer and dentin interface when controls and D-NPs were applied, after 6 m time point (Figures S5A and S5C). Samples treated with undoped NPs showed the NPs intimately close to the collagen fibers, and tubules appeared with a robust peritubular dentin ring (Figure S5B).

FIGURE 5

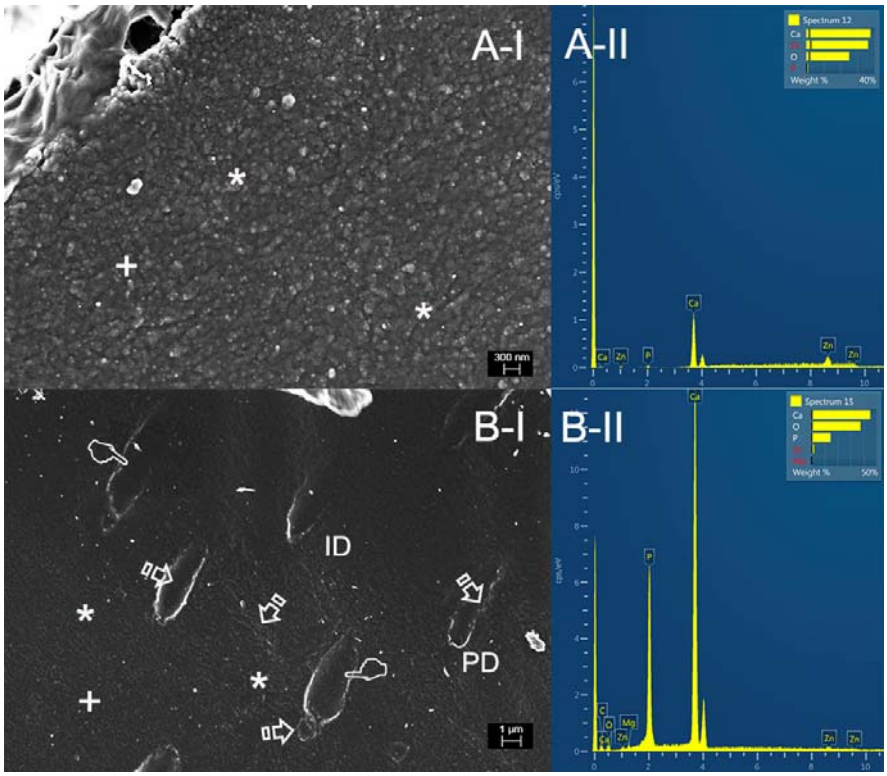

Figure 5. (**A)** FESEM image of apical root dentin treated with Ca-NPs at 6 m of storage. A mineral deposition is completely covering the dentin surface. Dentin resulted totally mineralized and the mineral formations did not allow any display of the entrance of the dentinal tubules. Intertubular dentin appeared entirely remineralized (asterisks) (**A·I**). (**B**) FESEM image of apical root dentin treated with Zn-NPs at 6 m of storage. The dentin surface exhibited multiple amorphous clumps of buttons-like materials, rounding or amorphous (asterisks). Dentin tubules appeared completely filled (pointers), and intertubular (ID) and peritubular (PD) dentin were entirely remineralized (**B·I**). **A·II** and **B·II** shown **s**pectra from energy dispersive analysis, attained at presented zones, (corresponding with the sign "+" at the images). Elemental composition of phosphorous (P), calcium (Ca), and zinc (Zn) as main components were encountered.

After 6 m, TEM analysis of the cervical dentin section that was treated with Ca-NPs exhibited, in bright-field (BF), a block-like of squared and triangular crystallite morphology (Figure S6A), more amorphous in nature (Figure S6B), while Zn-NPs-treated dentin showed, at the apical location, typical polymorph/polyhedral apatite crystals (Figures S6C and S6E). Zn-NPs, at the apical dentin surfaces promoted the formation of poorly-domain polycrystalline lattices of overlapped minerals of crystalline structure (Figures S6D and S6F).

Statistical results attained from the different ANOVA models are summarized in Table S3.

4. Discussion

Zn-NPs application, at the endodontic treatment previous to the sealing step, is recommended due to the attained lowest microleakage values and the increase of functional dentin remineralization. This remineralization totally covered the dentin surface occluding cracks, porosities and dentinal tubules; also producing reinforcement of mechanical properties of radicular dentin.

The improvement in the sealing ability that was attained by undoped NPs, Zn-NPs and Ca-NPs-treated root dentin (Figure 1) is related to hydroxyapatite formation (Figures 2A, 2B and S2B) that may close voids, capillary channels and pores (Gandolfi et al., 2007) through calcium-phosphate salts deposits (Figures 5A·II and 5B·II). These outcomes complied with higher fibrils width values at any dentin zone, (Table 2) (Figures 2A and 2B) after particle binding to the partially demineralized collagen. NPs collagen binding is probably required to perform a correct remineralization effect (Besinis et al., 2014, 2012) (Figure S5B). Enhanced remineralization of Ca-NPs has been proved (Toledano et al., 2017a), as it was not observed any demineralized collagen or empty dentinal tubules after treating root dentin (Figure 5A). Tested NPs had a diameter of about 100 nm, preventing them from passing into dentin trough interfibrillar space widths. Moreover, deeper infiltrative capability into the demineralized dentin is reduced because of particle binding to collagen (Besinis et al., 2014, 2012). Inside the dentinal tubules, particles were also observed without agglomerate due to their negative zeta potential (Osorio et al., 2016a). Dentin samples infiltrated with Zn-NPs displayed an extension of mineral

precipitate clusters through the thick network of crystals, located at intertubular dentin and at all tubules' lumen (Figure 5B).

The increase on fibrils width, therefore, and the remineralization of dentin are processes commonly associated (Clarkson et al., 1993). The highest intensity in both phosphate peak/area and crosslinking of collagen at cervical dentin was achieved by Ca-NPs-treated samples (Figure 3A), meanwhile Zn-NPs-treated ones obtained maximum values at apical dentin. This denoted major presence of calcium phosphate (Table 2) (Figure 3B). The high levels obtained for collagen cross-linking could be the basis for the improvement of mechanical properties of dentin (Toledano et al., 2019a). The lowest FWHM was, in general, obtained by Ca-NPs and Zn-NPs-treated dentin (Table S2). A narrower spectral peak width indicates a higher mineral crystallinity degree (Karan et al., 2009) (Figure S6A, S6C and S6E). Hence, Ca-NPs or Zn-NPs showed a great ability for the occlusion of dentinal tubules. Both kind of doped NPs application must be considered as a viable alternative for the promotion of radicular dentin sealing, as they produce the occlusion of dentinal tubules due to crystalline calcium-phosphate precipitation.

Heterogeneity in the distribution of mechanical properties between cervical and apical root dentin was observed at the Nano-DMA analysis. The complex modulus (E^*) is a value that quantifies the material resistance to dynamic deformation (Ryou et al., 2013). E^* differences between Zn-NPs-treated cervical and Zn-NPs-treated apical root dentin were higher (~3.76 fold) than when Ca-NPs were employed (~1.09 fold), at 6 m storage (Table 1). Zones of stress concentration, as crack deflections were formed and shown as crystal precipitated perpendicular to the peritubular dentin (asterisks), when Zn-NPs were applied at apical root dentin (Figures 2C and S1A). Ca-NPs-treated dentin surfaces barely displayed zones and signs of stress concentration (Figures 2A and S1B), caused by the homogeneity of viscoelastic properties (Agrawal et al., 2013) between cervical and apical

dentin. Thereby, the energy excess can be dissipated through tissue cracking in the zone of stress concentration if the energy stored at dentin is too great, generating viscoelastic-related morphological changes, with clinical implications, at dentin (Toledano et al., 2017a). Texture is defined as the distribution of crystallographic orientation of a polycrystalline specimen; it balances for changes in microstructure, evidencing a great influence on materials properties, as cracking resistance (Liss et al., 2003). Texture indices (R_{hkl}) in dentin polycrystalline structures were obtained affording to Eq. (3). For $R \approx 1$, the grains were counted randomly oriented (Xue et al., 2013). If R value is greater or lower than 1.0, it indicates the existence of preferred grain orientation or texture (Low, 2004). In 310 planes at cervical dentin, Ca-NPs samples attained the closest values to this number, after 6 m storage, (1.163) (Table S2); it implies reinforcement in dentin crack resistance.

Topography mapping achieved with AFM allowed to obtain a neat stick-slip image at the cervical/apical root dentin in Zn-NPs treated samples at 6 m storage time (Figure 2C). These stick-slip images and little rod-like minerals seemed as bridge-like structures at the surface of the dentin (Agrawal et al., 2013). These slipped mineralized dentin bridges can determine the effectively resisting crack propagation that leads to a fracture (Shinno et al., 2016), by nucleating minerals at micro and nano-scale damage zones. When Zn-NPs were applied, it is speculated that this stick-slips formation on dentin depends on the Zn^{++} existence in the chemical formulation of the NP, which produced new crystals precipitation (Toledano-Osorio et al., 2018b). Sticks-slips formation may also be due to the relative amorphizacion of the mineral substrate (Table S2) (Figures 2A, S6D and S6F) as it provides ions for reparation and remineralization of dentin (Chen et al., 2014). These mineral precipitations were shown as multiple rod-like structures adjoining the

intratubular crystals and at peritubular dentin (Figure 2C), and were no present in Ca-NPs-treated samples (Figure 2A).

The general improvement of *Ei* at root dentin (inter- and peri-tubular) surfaces (cervical and apical) when Zn-NPs were placed and measured after 6 m of storage (Table 1), may be associated with a functional remineralizing outcome (Bertassoni et al., 2012; Toledano et al., 2017a). A qualitative assessment of the size of the logically scattering domain (*i.e.* the crystallite size) is shown in Table S2. A raise of the mean crystallite size (~1.04 fold) along a direction parallel and perpendicular to the *c*-axis [τ_{002} (*H*)] and [τ_{310} (*L*), respectively] was obtained when cervical dentin surfaces were treated with Zn-NPs (Table S2). In calcified tissues, crystallite size has been shown to increase with tissue maturation (Gawda et al., 2004; Hanschin and Stern, 1995), which is linked to low nanoroughness (Zurick et al., 2013), interfibrillar remineralization (Bertassoni et al., 2012) and crystallinity (Olszta et al., 2007) (Figures S6C and S6E). The analysis of μXRD^2 profiles confirmed higher intensities of samples treated with Zn-NPs at 002 peak at cervical dentin (Figure 4A) and at 211 and 112 peaks at apical dentin (Figure 4B), where diffractography patterns show HAp presence (blue bars) with sharp and narrow crystalline peaks. Similarly, brighter rings were observed at the diffraction analysis, *i.e*, higher crystallinity, than in the rest of the samples after the use of Zn-NPs (Figure S4E). Therefore, as cervical root dentin is considered a potential failure site due to strain, deformation and stress concentration (Kaushik et al., 2018); the use of Zn-NPs should be indicated in endodontics.

The mineral deposition became favored by the presence of Zn^{2+}, which probably performed as Ca/P growth inhibitor (Hoppe et al., 2011; Toledano et al., 2015). On the contrary, root dentin generally diminished its *Ei* values over time when Ca-NPs were employed as canal sealer at both cervical and apical dentin disks (Table 1), indicating

poor remineralization capability at the intrafibrillar compartment after 6 m time. The highest relative mineral concentration (RMC) (Table 2) and the lowest *Ei* (Table 1) that was obtained after treating dentin with Ca-NPs indicates that the relative degree of mineral gain was at the expenses of non-functional dentin remineralization, *i.e*, extrafibrillar mineralization (Bertassoni et al., 2012), slowing down the remodeling of active dentin, with a decrease in maturity (Figures S6A and S6B) and low mechanical properties (Toledano et al., 2017a). This XRD amorphous dentin (Table S2) features more crystals defects in nanocrystallite structures, *i.e,* minor crystallite size (20.57 nm long, 5.86 nm width) and lattice distortion (Zhang et al., 2003) with increased microstrain values (Table S2) (Moshaverinia et al., 2008). These outcomes discouraged its indication as canal sealer, and Zn-NPs are preferred.

Root dentin treated with D-NPs achieved both the best nature of collagen and α-helices values (Table 2). This indicated the best organization, quality and an improved structure of collagen (Bakland and Andreasen, 2012; Salehi et al., 2013). Nevertheless, D-NPs revealed higher microleakage values (Figure 1) due to multiple intratubular voids and formed porosities (Figures S2C and S5C), meaning poor sealing ability. Therefore, D-NPs must be discarded to improve the sealing or dentin remineralization during the endodontical treatment.

There are some constraints to this experiment. It does not show the long-term effect of NPs, as a 6 m study. To ascertain if the present *in vitro* results could be extrapolated into profits for patients will require clinical studies. Future research should also include the morpho-physico-chemically characterization of these treated surfaces using X-ray fluorescence microscopy studies and X-ray micro-computed tomography.

5. Conclusions

Sealing and remineralization of the radicular dentin was not efficient when using D-NPs. Non-functional remineralization was produced by Ca-NPs, based on the new deposits of imperfect and immature nanocrystallite dentin structures. The highest sealing ability was exhibited by Zn-NPs-treated specimens. The low microleakage values among groups were consistent with the highest modulus of Young and dentin mineralization that were also attained with Zn-NPs. This performance may be explained by the occlusion of dentinal tubules, cavities, pores, capillary channels and cracks. Thereby, within the limitations of the present study, application of Zn-NPs is encouraged due to its mechanical reinforcing capability at root dentin and to its enhanced durable sealing ability.

Acknowledgements

This work was supported by the Ministry of Economy and Competitiveness and European Regional Development Fund [MAT2017-85999P MINECO/AEI/FEDER/UE]. The authors affirm that no actual or potential conflict of interest including any financial, personal or other relationships with other people or organizations within three years of beginning the submitted work that could inappropriately influence, or be perceived to influence, their work. Any other potential conflict of interest is disclosed.

References

Agarwal, A., Bhattacharya, H.S., Srikanth, G., Singh, A., 2013. Comparative evaluation of decalcified freeze dried bone allograft with and without local doxycycline in non-contained human periodontal infrabony defects. J. Indian Soc. Periodontol. 17, 490–494. https://doi.org/10.4103/0972-124X.118322

Ager, J.W., Nalla, R.K., Breeden, K.L., Ritchie, R.O., 2005. Deep-ultraviolet Raman spectroscopy study of the effect of aging on human cortical bone. J. Biomed. Opt. 10, 034012. https://doi.org/10.1117/1.1924668

Agrawal, R., Nieto, A., Chen, H., Mora, M., Agarwal, A., 2013. Nanoscale damping characteristics of boron nitride nanotubes and carbon nanotubes reinforced polymer composites. ACS Appl. Mater. Interfaces 5, 12052–12057. https://doi.org/10.1021/am4038678

Bakland, L.K., Andreasen, J.O., 2012. Will mineral trioxide aggregate replace calcium hydroxide in treating pulpal and periodontal healing complications subsequent to dental trauma? A review. Dent. Traumatol. 28, 25–32. https://doi.org/10.1111/j.1600-9657.2011.01049.x

Batool, F., Strub, M., Petit, C., Bugueno, I.M., Bornert, F., Clauss, F., Huck, O., Kuchler-Bopp, S., Benkirane-Jessel, N., 2018. Periodontal Tissues, Maxillary Jaw Bone, and Tooth Regeneration Approaches: From Animal Models Analyses to Clinical Applications. Nanomaterials 8, 337. https://doi.org/10.3390/nano8050337

Bertassoni, L.E., Stankoska, K., Swain, M.V., 2012. Insights into the structure and composition of the peritubular dentin organic matrix and the lamina limitans. Micron 43, 229–236. https://doi.org/10.1016/j.micron.2011.08.003

Besinis, A., van Noort, R., Martin, N., 2014. Remineralization potential of fully demineralized dentin infiltrated with silica and hydroxyapatite nanoparticles. Dent. Mater. 30, 249–262. https://doi.org/10.1016/j.dental.2013.11.014

Besinis, A., van Noort, R., Martin, N., 2012. Infiltration of demineralized dentin with silica and hydroxyapatite nanoparticles. Dent. Mater. 28, 1012–1023. https://doi.org/10.1016/j.dental.2012.05.007

Bouillaguet, S., Shaw, L., Barthelemy, J., Krejci, I., Wataha, J.C., 2008. Long-term sealing ability of Pulp Canal Sealer, AH-Plus, GuttaFlow and Epiphany. Int Endod. J. 41, 219–226. https://doi.org/10.1111/j.1365-2591.2007.01343.x

Brosh, T., Metzger, Z., Pilo, R., 2018. Circumferential root strains generated during lateral compaction with stainless steel vs. nickel-titanium finger spreaders. Eur. J. Oral Sci. 126, 518–525. https://doi.org/10.1111/eos.12569

Chen, C., Liu, J., Sun, F., Stansbury, J.W., 2014. Tuning Surface Microstructure and Gradient Property of Polymer by Photopolymerizable Polysiloxane-modified Nanogels. RSC Adv. 4, 28928–28936. https://doi.org/10.1039/C4RA02176B

Chieruzzi, M., Pagano, S., Moretti, S., Pinna, R., Milia, E., Torre, L., Eramo, S., 2016. Nanomaterials for Tissue Engineering In Dentistry. Nanomaterials 6, 134. https://doi.org/10.3390/nano6070134

Clarkson, B.H., McCurdy, S.P., Gaz, D., Hand, A.R., 1993. Effects of phosphoprotein on collagen fibril formation in vitro. Arch. Oral Biol. 38, 737–743. https://doi.org/10.1016/0003-9969(93)90068-W

Fontana, M., Young, D.A., Wolff, M.S., Pitts, N.B., Longbottom, C., 2010. Defining dental caries for 2010 and beyond. Dent. Clin. North Am. 54, 423–440. https://doi.org/10.1016/j.cden.2010.03.007

Gandolfi, M.G., Sauro, S., Mannocci, F., Watson, T.F., Zanna, S., Capoferri, M., Prati, C., Mongiorgi, R., 2007. New tetrasilicate cements as retrograde filling material: an in vitro study on fluid penetration. J. Endod. 33, 742–745. https://doi.org/10.1016/j.joen.2007.02.008

Gawda, H., Sękowski, L., Trębacz, H., 2004. In vitro examination of human teeth using ultrasound and X-ray diffraction. Acta Bioeng. Biomech. Vol. 6, 41–49.

Habelitz, S., Balooch, M., Marshall, S.J., Balooch, G., Marshall, G.W., 2002. In situ atomic force microscopy of partially demineralized human dentin collagen fibrils. J. Struct. Biol. 138, 227–236.

Hakki, S.S., Bozkurt, B.S., Ozcopur, B., Gandolfi, M.G., Prati, C., Belli, S., 2013. The response of cementoblasts to calcium phosphate resin-based and calcium silicate-based commercial sealers. Int. Endod. J. 46, 242–252. https://doi.org/10.1111/j.1365-2591.2012.02122.x

Hanschin, R.G., Stern, W.B., 1995. X-ray diffraction studies on the lattice perfection of human bone apatite (Crista iliaca). Bone 16, 355S-363S.

Hoppe, A., Güldal, N.S., Boccaccini, A.R., 2011. A review of the biological response to ionic dissolution products from bioactive glasses and glass-ceramics. Biomaterials 32, 2757–2774. https://doi.org/10.1016/j.biomaterials.2011.01.004

Karan, K., Yao, X., Xu, C., Wang, Y., 2009. Chemical profile of the dentin substrate in non-carious cervical lesions. Dent. Mater. 25, 1205–1212. https://doi.org/10.1016/j.dental.2009.04.006

Kaushik, M., Kumar, U., Sharma, R., Mehra, N., Rathi, A., 2018. Stress distribution in endodontically treated abfracted mandibular premolar restored with different cements and crowns: A three-dimensional finite element analysis. J. Conserv. Dent. 21, 557–561. https://doi.org/10.4103/JCD.JCD_206_18

Kinney, J.H., Marshall, S.J., Marshall, G.W., 2003. The mechanical properties of human dentin: a critical review and re-evaluation of the dental literature. Crit. Rev. Oral Biol. Med. 14, 13–29.

Liss, K.-D., Bartels, A., Schreyer, A., Clemens, H., 2003. High-energy X-rays: a tool for advanced bulk investigations in materials science and physics. Texture. Microstruct. 35, 219–252. https://doi.org/10.1080/07303300310001634952

Low, I.-M., 2004. Depth-Profiling of Crystal Structure, Texture, and Microhardness in a Functionally Graded Tooth Enamel. J. Am. Ceram. Soc. 87, 2125–2131. https://doi.org/10.1111/j.1151-2916.2004.tb06369.x

Maret, W., 2013. Zinc Biochemistry: From a Single Zinc Enzyme to a Key Element of Life12. Adv. Nutr. 4, 82–91. https://doi.org/10.3945/an.112.003038

Marshall, G.W., Marshall, S.J., Kinney, J.H., Balooch, M., 1997. The dentin substrate: structure and properties related to bonding. J. Dent. 25, 441–458.

Medina-Castillo, A.L., Fernandez-Sanchez, J.F., Segura-Carretero, A., Fernandez-Gutierrez, A., 2010. Micrometer and Submicrometer Particles Prepared by Precipitation Polymerization: Thermodynamic Model and Experimental Evidence of the Relation between Flory's Parameter and Particle Size. Macromolecules 43, 5804–5813. https://doi.org/10.1021/ma100841c

Mestres, G., Aguilera, F.S., Manzanares, N., Sauro, S., Osorio, R., Toledano, M., Ginebra, M.P., 2014. Magnesium phosphate cements for endodontic applications with improved long-term sealing ability. Int. Endod. J. 47, 127–139. https://doi.org/10.1111/iej.12123

Monticelli, F., Osorio, R., Toledano, M., Ferrari, M., Pashley, D.H., Tay, F.R., 2010. Sealing properties of one-step root-filling fibre post-obturators vs. two-step

delayed fibre post-placement. J. Dent. 38, 547–552. https://doi.org/10.1016/j.jdent.2010.03.014

Monticelli, F., Sword, J., Martin, R.L., Schuster, G.S., Weller, R.N., Ferrari, M., Pashley, D.H., Tay, F.R., 2007. Sealing properties of two contemporary single-cone obturation systems. Int. Endod. J. 40, 374–385. https://doi.org/10.1111/j.1365-2591.2007.01231.x

Moshaverinia, A., Ansari, S., Moshaverinia, M., Roohpour, N., Darr, J.A., Rehman, I., 2008. Effects of incorporation of hydroxyapatite and fluoroapatite nanobioceramics into conventional glass ionomer cements (GIC). Acta Biomater 4, 432–440. https://doi.org/10.1016/j.actbio.2007.07.011

Negi, H., Saikia, S.K., Kanaujia, R., Jaiswal, S., Pandey, R., 2017. 3β-Hydroxy-urs-12-en-28-oic acid confers protection against ZnONPs induced adversity in Caenorhabditis elegans. Environ. Toxicol. Pharm. 53, 105–110. https://doi.org/10.1016/j.etap.2017.05.004

Olszta, M.J., Cheng, X., Jee, S.S., Kumar, R., Kim, Y.-Y., Kaufman, M.J., Douglas, E.P., Gower, L.B., 2007. Bone structure and formation: A new perspective. Mat Sci Eng R 58, 77–116. https://doi.org/10.1016/j.mser.2007.05.001

Osorio, R., Alfonso-Rodríguez, C.A., Medina-Castillo, A.L., Alaminos, M., Toledano, M., 2016a. Bioactive Polymeric Nanoparticles for Periodontal Therapy. PLoS ONE 11, e0166217. https://doi.org/10.1371/journal.pone.0166217

Osorio, R., Cabello, I., Medina-Castillo, A.L., Osorio, E., Toledano, M., 2016b. Zinc-modified nanopolymers improve the quality of resin-dentin bonded interfaces. Clin. Oral Investig. 20, 2411–2420. https://doi.org/10.1007/s00784-016-1738-y

Patil, P., Banga, K.S., Pawar, A.M., Pimple, S., Ganeshan, R., 2017. Influence of root canal obturation using gutta-percha with three different sealers on root

reinforcement of endodontically treated teeth. An in vitro comparative study of mandibular incisors. J. Conserv. Dent. 20, 241–244. https://doi.org/10.4103/JCD.JCD_233_16

Perales, F., Agulló-Rueda, F., Lamela, J., Heras, C. de las, 2008. Optical and structural properties of Sb2S3/MgF2 multilayers for laser applications. J. Phys. D: Appl. Phys. 41, 045403. https://doi.org/10.1088/0022-3727/41/4/045403

Rodriguez-Navarro, A.B., 2007. Registering pole figures using an X-ray single-crystal diffractometer equipped with an area detector. J. Appl. Crystallogr. 40, 631–634. https://doi.org/10.1107/S0021889807014574

Ryou, H., Pashley, D.H., Tay, F.R., Arola, D., 2013. A characterization of the mechanical behavior of resin-infiltrated dentin using nanoscopic Dynamic Mechanical Analysis. Dent. Mater. 29, 719–728. https://doi.org/10.1016/j.dental.2013.03.022

Salehi, H., Terrer, E., Panayotov, I., Levallois, B., Jacquot, B., Tassery, H., Cuisinier, F., 2013. Functional mapping of human sound and carious enamel and dentin with Raman spectroscopy. J. Biophotonics 6, 765–774. https://doi.org/10.1002/jbio.201200095

Sánchez, M.C., Toledano-Osorio, M., Bueno, J., Figuero, E., Toledano, M., Medina-Castillo, A.L., Osorio, R., Herrera, D., Sanz, M., 2019. Antibacterial effects of polymeric PolymP-n Active nanoparticles. An in vitro biofilm study. Dent. Mater. 35, 156–168. https://doi.org/10.1016/j.dental.2018.11.015

Shinno, Y., Ishimoto, T., Saito, M., Uemura, R., Arino, M., Marumo, K., Nakano, T., Hayashi, M., 2016. Comprehensive analyses of how tubule occlusion and advanced glycation end-products diminish strength of aged dentin. Sci. Rep. 6, 19849. https://doi.org/10.1038/srep19849

Takeyasu, K., Omote, H., Nettikadan, S., Tokumasu, F., Iwamoto-Kihara, A., Futai, M., 1996. Molecular imaging of Escherichia coli F0F1-ATPase in reconstituted membranes using atomic force microscopy. FEBS Lett. 392, 110–113.

Toledano, M., Aguilera, F.S., Osorio, E., Cabello, I., Toledano-Osorio, M., Osorio, R., 2015. Self-etching zinc-doped adhesives improve the potential of caries-affected dentin to be functionally remineralized. Biointerphases 10, 031002. https://doi.org/10.1116/1.4926442

Toledano, M., Cabello, I., Osorio, E., Aguilera, F.S., Medina-Castillo, A.L., Toledano-Osorio, M., Osorio, R., 2019a. Zn-containing polymer nanogels promote cervical dentin remineralization. Clin. Oral Invest. 23, 1197–1208. https://doi.org/10.1007/s00784-018-2548-1

Toledano, M., Muñoz-Soto, E., Aguilera, F.S., Osorio, E., González-Rodríguez, M.P., Pérez-Álvarez, M.C., Toledano-Osorio, M., Osorio, R., 2019b. A zinc oxide-modified hydroxyapatite-based cement favored sealing ability in endodontically treated teeth. J. Dent. 88, 103162. https://doi.org/ 10.1016/j.jdent.2019.06.009

Toledano, M., Muñoz-Soto, E., Aguilera, F.S., Osorio, E., Pérez-Álvarez, M.C., García-Menocal, J.AD., Toledano-Osorio, M., Osorio, R., 2019c. The mineralizing effect of zinc oxide-modified hydroxyapatite-based sealer on radicular dentin. Clin. Oral Invest. https://doi.org/10.1007/s00784-019-02938-5

Toledano, M., Osorio, R., Osorio, E., Medina-Castillo, A.L., Toledano-Osorio, M., Aguilera, F.S., 2017a. Ions-modified nanoparticles affect functional remineralization and energy dissipation through the resin-dentin interface. J Mech Behav Biomed Mater 68, 62–79. https://doi.org/10.1016/j.jmbbm.2017.01.026

Toledano, M., Osorio, R., Pérez-Álvarez, M.-C., Osorio, E., Lynch, C.-D., Toledano-Osorio, M., 2018. A zinc-doped endodontic cement facilitates functional

mineralization and stress dissipation at the dentin surface. Med. Oral Patol. Oral Cir. Bucal 23, e646–e655. https://doi.org/10.4317/medoral.22751

Toledano, M., Pérez-Álvarez, M.C., Aguilera, F.S., Osorio, E., Cabello, I., Toledano-Osorio, M., Osorio, R., 2017b. A zinc oxide-modified hydroxyapatite-based cement facilitated new crystalline-stoichiometric and amorphous apatite precipitation on dentine. Int. Endod. J. 50 Suppl 2, e109–e119. https://doi.org/10.1111/iej.12807

Toledano-Osorio, M., Babu, J.P., Osorio, R., Medina-Castillo, A.L., García-Godoy, F., Toledano, M., 2018a. Modified Polymeric Nanoparticles Exert In Vitro Antimicrobial Activity Against Oral Bacteria. Materials (Basel) 11. https://doi.org/10.3390/ma11061013

Toledano-Osorio, M., Osorio, E., Aguilera, F.S., Medina-Castillo, A.L., Toledano, M., Osorio, R., 2018b. Improved reactive nanoparticles to treat dentin hypersensitivity. Acta Biomater. 72, 371–380. https://doi.org/10.1016/j.actbio.2018.03.033

Torabinejad, M., Kutsenko, D., Machnick, T.K., Ismail, A., Newton, C.W., 2005. Levels of evidence for the outcome of nonsurgical endodontic treatment. J. Endodont. 31, 637–646.

Torabinejad, M., Watson, T.F., Pitt Ford, T.R., 1993. Sealing ability of a mineral trioxide aggregate when used as a root end filling material. J. Endodont. 19, 591–595. https://doi.org/10.1016/S0099-2399(06)80271-2

Vizgirda, P.J., Liewehr, F.R., Patton, W.R., McPherson, J.C., Buxton, T.B., 2004. A comparison of laterally condensed gutta-percha, thermoplasticized gutta-percha, and mineral trioxide aggregate as root canal filling materials. J Endodont. 30, 103–106. https://doi.org/10.1097/00004770-200402000-00010

Wang, C., Wang, Y., Huffman, N.T., Cui, C., Yao, X., Midura, S., Midura, R.J., Gorski, J.P., 2009. Confocal Laser Raman Microspectroscopy of Biomineralization Foci in UMR 106 Osteoblastic Cultures Reveals Temporally Synchronized Protein Changes Preceding and Accompanying Mineral Crystal Deposition. J. Biol. Chem. 284, 7100–7113. https://doi.org/10.1074/jbc.M805898200

Xue, J., Zavgorodniy, A.V., Kennedy, B.J., Swain, M.V., Li, W., 2013. X-ray microdiffraction, TEM characterization and texture analysis of human dentin and enamel. J. Microsc. 251, 144–153. https://doi.org/10.1111/jmi.12053

Yoo, Y.-J., Oh, J.-H., Zhang, Q., Lee, W., Woo, K.M., 2018. Dimethyloxalylglycine-embedded Poly(ε-caprolactone) Fiber Meshes Promote Odontoblastic Differentiation of Human Dental Pulp–derived Cells. J. Endodont. 44, 98-103.e1. https://doi.org/10.1016/j.joen.2017.09.002

Zhang, Z., Zhou, F., Lavernia, E.J., 2003. On the analysis of grain size in bulk nanocrystalline materials via x-ray diffraction. Metall. Mater. Trans. A 34, 1349–1355. https://doi.org/10.1007/s11661-003-0246-2

Zheng, J., Wu, Z., Niu, K., Xie, Y., Hu, X., Fu, J., Tian, D., Fu, K., Zhao, B., Kong, W., Sun, C., Wu, L., 2019. Microbiome of Deep Dentinal Caries from Reversible Pulpitis to Irreversible Pulpitis. J. Endodont. 45, 302-309.e1. https://doi.org/10.1016/j.joen.2018.11.017

Zurick, K.M., Qin, C., Bernards, M.T., 2013. Mineralization Induction Effects of Osteopontin, Bone Sialoprotein, and Dentin Phosphoprotein on a Biomimetic Collagen Substrate. J. Biomed. Mater. Res. A 101, 1571–1581. https://doi.org/10.1002/jbm.a.34462

APPENDIX A. SUPPLEMENTARY DATA

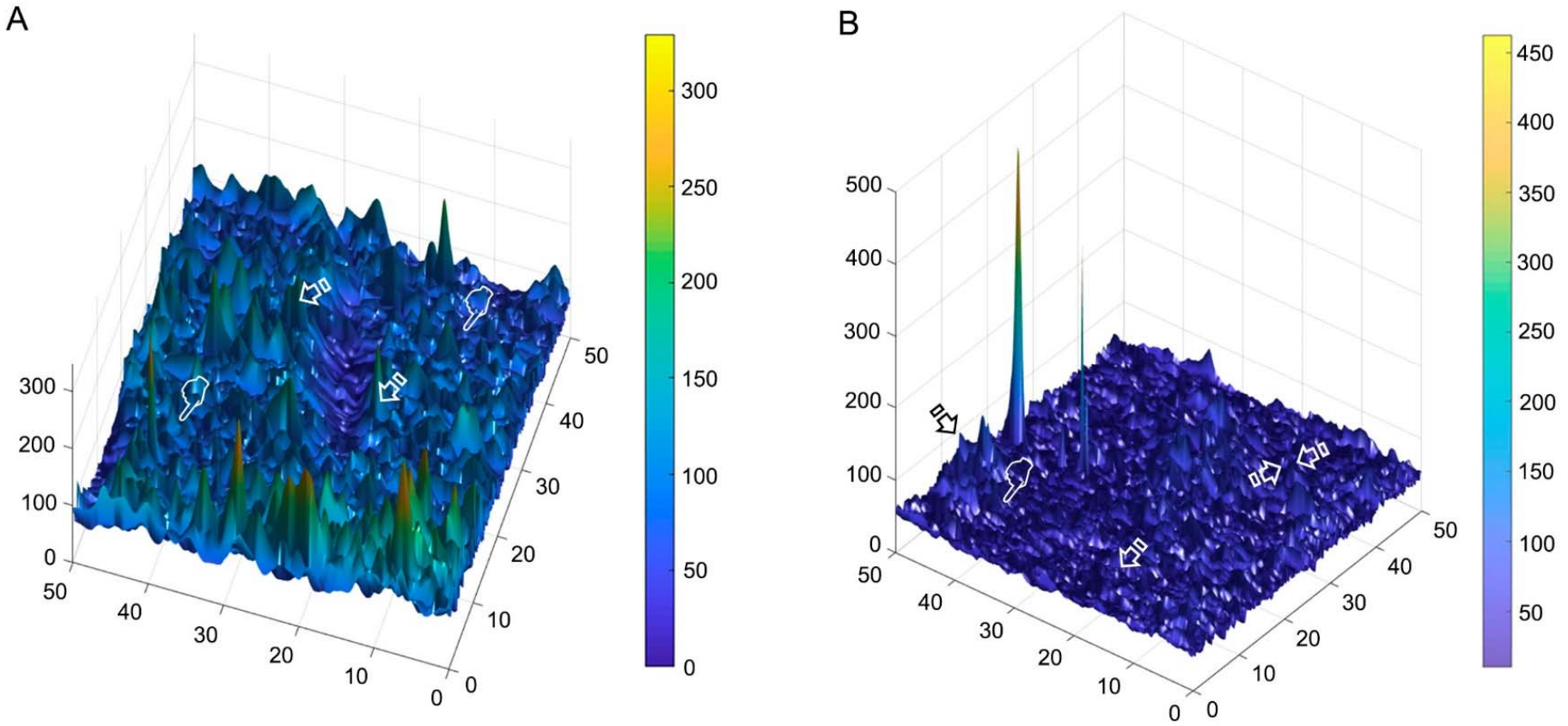

Figure S1. (**A**) 3D contour map of the complex modulus (*E**) at the apical root dentin treated with Zn-NPs, achieved at 6 m time point. Numerical data associate the clear blue and dark blue colors with both peritubular and intertubular dentin viscoelastic behavior, respectively. In the color scheme displayed, the clear greenish-blue color is associated to the highest value of the locally measured moduli, likely corresponding to the highest resistance to deformation of the peritubular dentin (arrows). (**B**) 3D contour map of the complex modulus (*E**) at the cervical root dentin treated with Ca-NPs, obtained at 6 m storage. In the color scheme displayed, the clear blue color is associated to the highest value of the locally measured moduli, likely corresponding to the highest resistance to deformation of the peritubular dentin (arrows). *E** of the intertubular dentin is shown in darker blue color (pointers). The pixel data array at the mapping is shown according to *E** distribution that happens with a clear separation between intertubular and peritubular dentin (faced arrows).

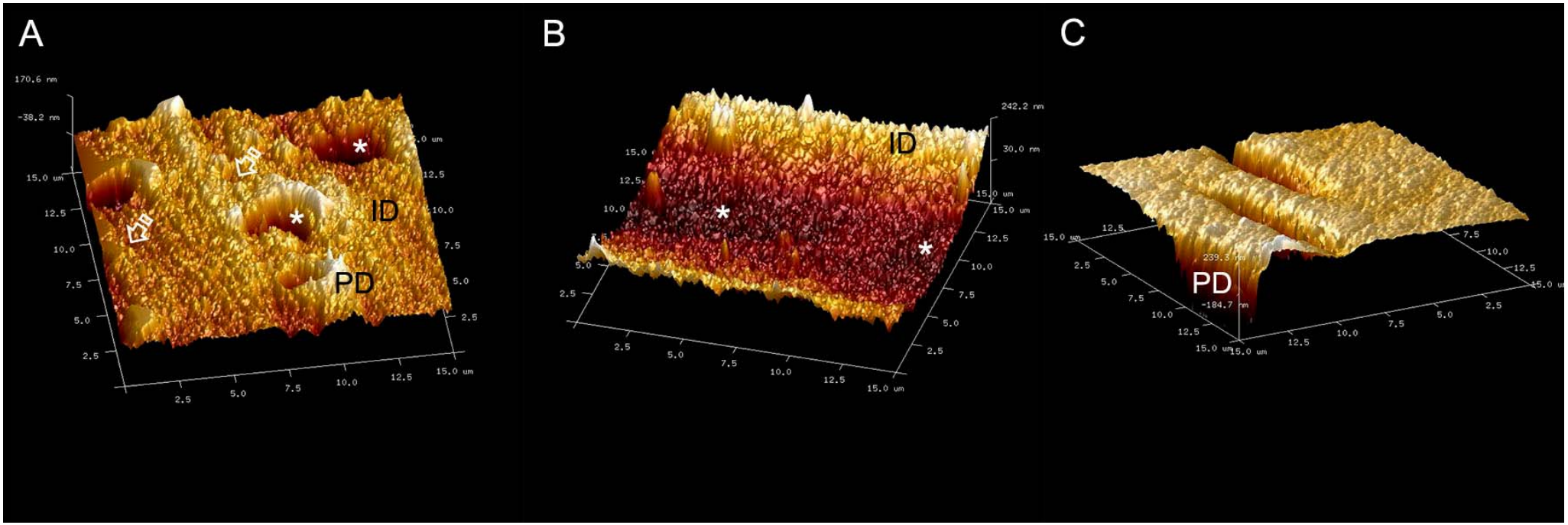

Figure S2. (**A**) 15 x 15 µm topographic mapping obtained by AFM at the inner zone of the cervical dentin at control group, after 6 m of storage. Open tubules were observed (asterisks). The peritubular (PD) dentin ring was evident. Multiple pores (arrows) characterized the intertubular dentin (ID). (**B**) 15 x 15 µm topographic mapping obtained by AFM at the inner zone of the apical dentin treated with undoped NPs, after 6 m of storage. Tubules were mineral-filled with porosities in the surface (asterisks). Intertubular dentin (ID) appeared mineralized. (**C**) 15 x 15 µm topographic mapping obtained by AFM at the inner zone of the cervical dentin treated with D-NPs, after 6 m of storage. Peritubular dentin (PD) was clearly visible. Tubules were open. No signs of mineralization were adverted.

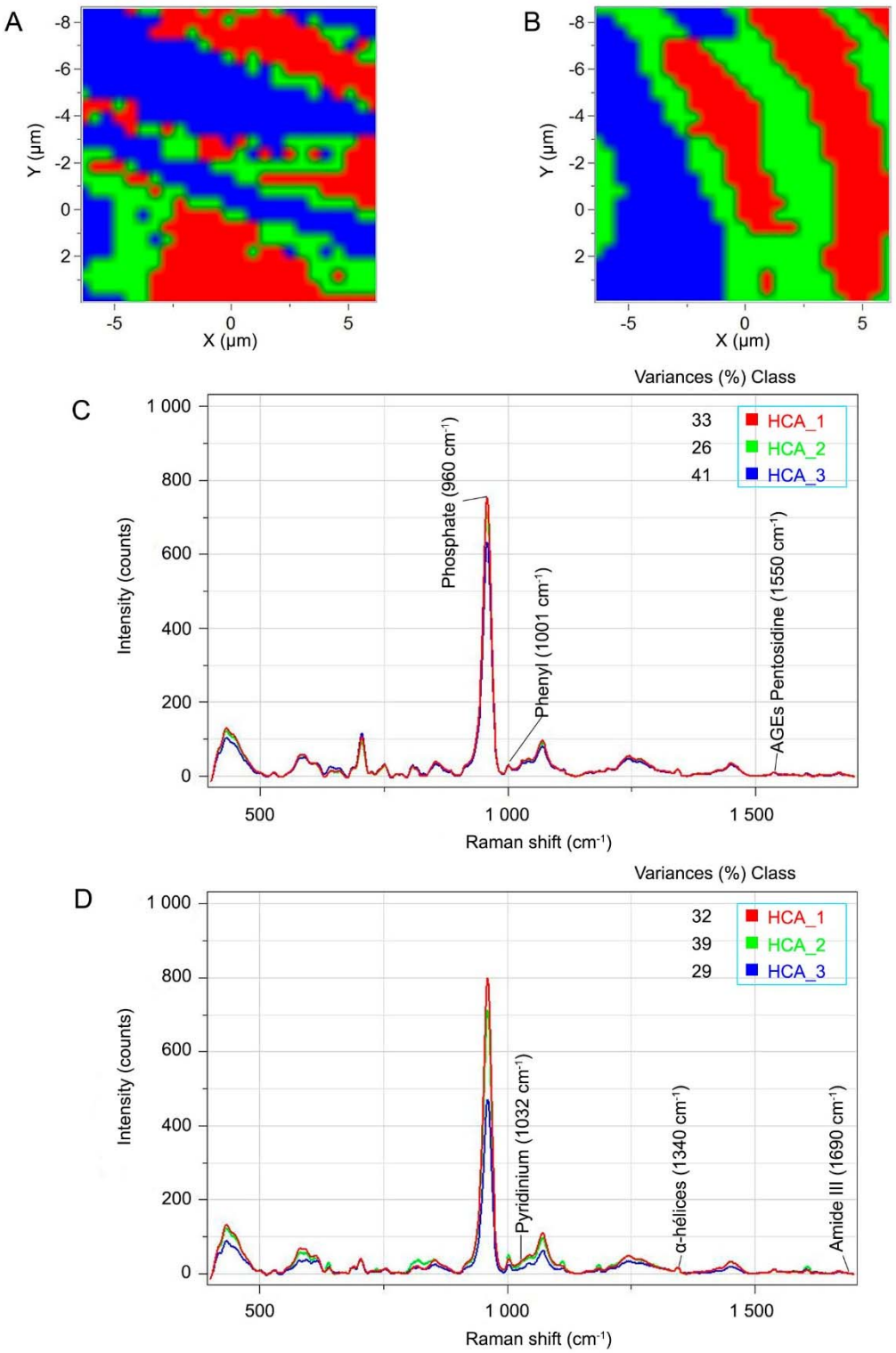

Figure S3. Colour mapping from hierarchical cluster analysis **(**HCA) images corresponding to dentin after treatment with Ca-NPs (**A**) and Zn-NPs (**B**), both in similar conditions to those reflected in Figures 3A and 3B. Three levels of HCA clustering are shown. Areas of distinct colour have differences in Raman spectral distribution and chemical composition. Each cluster, corresponding to a different dentin remineralization stage, is assigned to a different colour (red, green, and blue), thus obtaining a false colour-image of the substrate on the basis of similar spectral features. Spectra from hierarchical cluster analysis (HCA) results of dentin surfaces treated with Ca-NPs (**C**) and Zn-NPs (**D**) both in similar conditions to those reflected in Figures 3A and 3B.

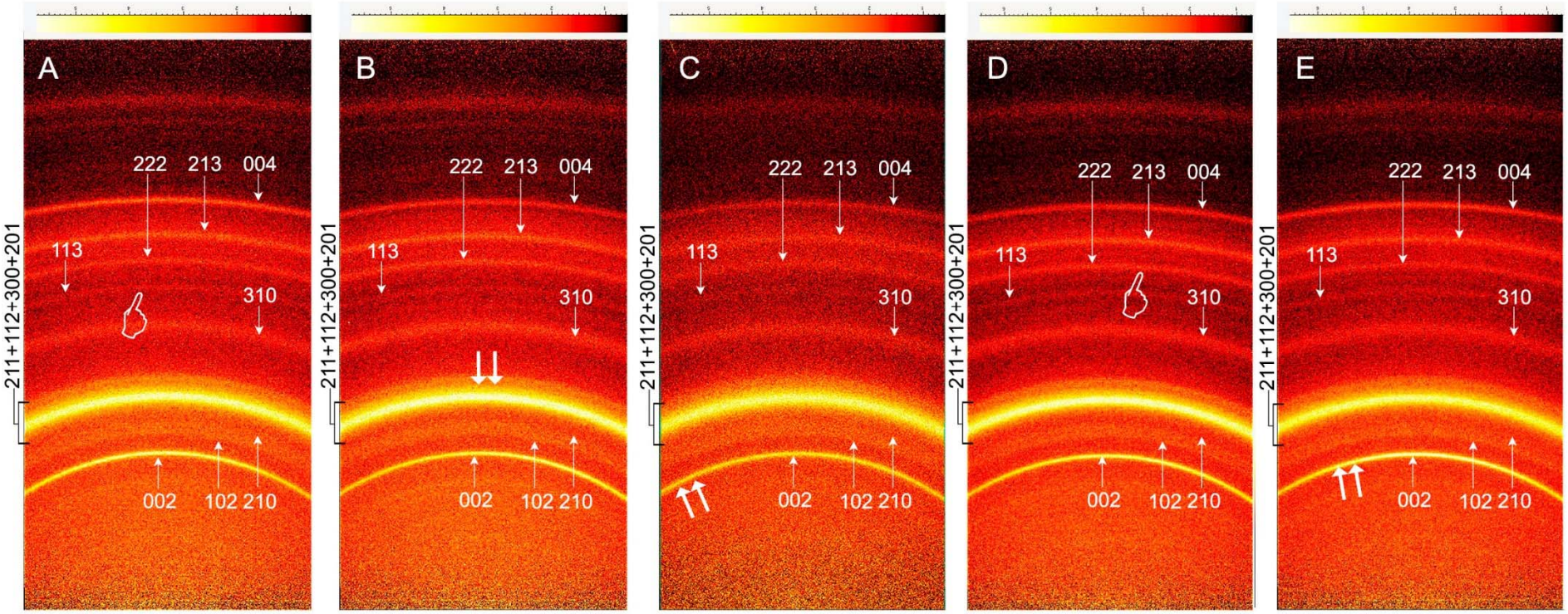

Figure S4. Debye-Scherrer rings of the inner zones of the apical (A, B and D) and cervical (C and E) root dentin after 6 m for each experimental group: Control (**A**), undoped NP (**B**), D-NPs (**C**), Ca-NPs (**D**) and Zn-NPs (**E**). Pointers and double arrows mean weak and strong diffraction rings, respectively.

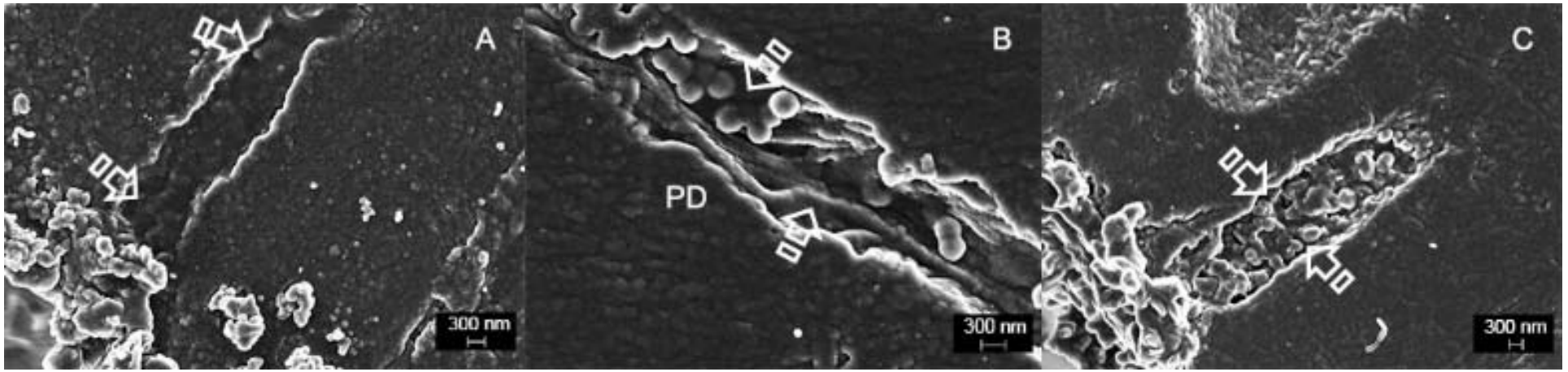

Figure S5. Representative FESEM images of apical root dentin in control (**A**) and cervical root dentin in unloaded NPs (**B**) after 6 m of storage. Dentinal tubules were partially mineral filled, allowing multiple empty spaces and porosities (arrows). Some tubules appeared partially mineral free with NPs intimately close to the collagen fibers, and with a robust peritubular dentin wall (**B**). At cervical root dentin in D-NPs group (**C**) mineral exhibited multiform clumps of material scattered, uneven, grouped or interconnected as dense network of buttons-like materials, rounding or amorphous, which can also be observed in control samples (**A**).

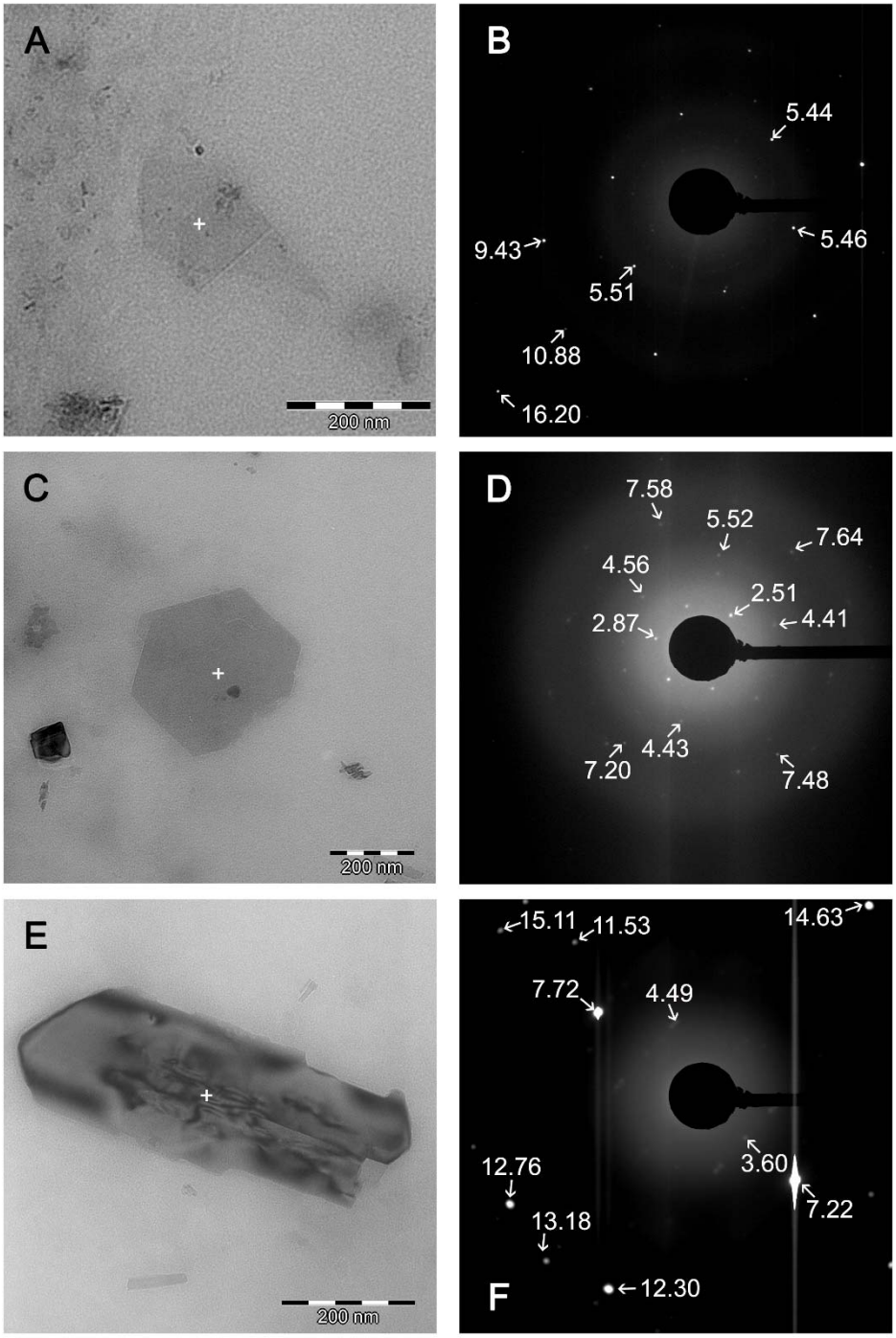

Figure S6. (**A**) Bright-field of an assembly of a block-like or squared apatite crystals of apical root dentin, treated with Ca-NPs, after 6 m storage. It is observed that the particles have a domain of locally aligned crystal arrays, showing the staggered order of polygon crystallites (scale bar: 200 nm). (**B**) Diffractography from the selected area electron diffraction (SAED) d-values of submicron size (+) depicts diffuse halo rings, indicating the presence of amorphous structure. **(C, E)** Bright-field of an assembly of hexagonal and polyhedral apatite crystals, respectively, of cervical root dentin treated with Zn-NPs, after 6 m storage. The minerals have scarce domains of locally aligned crystal arrays (scale bar: 200 nm). (**D, F)** Selected area electron diffraction (SAED) pattern containing differentiated halo rings and clear *d* spacing values, meaning the presence of remnant crystallite matter. Peripheral diffuse halo rings can be noted at the external orbits of the SAED indicating complementary amorphous structure (distances are expressed in 1/nm).

Table S1. Mean and standard deviation (SD) of fiber diameter (nm) and nano – roughness (SRa-nm) measured by AFM at the different dentin surfaces.

	Fiber Diameter				**Nano – roughness**			
	Cervical		**Apical**		**Cervical**		**Apical**	
	24h	**6m**	**24h**	**6m**	**24h**	**6m**	**24h**	**6m**
Control	80.30 (3.98) Aa	78.37 (5.08) Aa	80.81 (4.02) Aa	74.27) (3.57) Aa	11.43 (1.81) Aa*	22.14 (3.14) Aa	7.02 (4.85) Aa*	18.69 (3.40) Aa
NPs	99.88 (8.93) Ba*	172.27 (11.43) Ca	95.90 (10.47) Ba*	169.12 (8.61) Ba	45.10 (4.40) Ba	39.09 (6.83) Ba	42.16 (6.25) Ba	39.02 (2.13) Ba
D-NPs	77.96 (1.84) Aa	78.05 (3.66) Aa	79.62 (5.75) Aa	82.20 (8.46) Aa	25.60 (3.87) Ca*	12.55 (3.74) Ca	25.21 (5.39) Ca*	14.66 (2.66) Aa
Ca-NPs	135.85 (14.45) Ca*	179.91 (6.44) BCa	118.83 (6.56) Ba*	184.00 (14.48) CBa	45.48 (6.31) Ba*	29.10 (4.15) Aa	50.66 (5.89) Ba*	23.79 (10.23) Aa
Zn-NPs	151.20 (7.52) Ca*	197.00 (10.08) Ba	151.61 (6.41) Ca*	194.47 (16.46) Ca	7.09 (1.24) Da	6.91 (3.41) Ca	9.00 (1.57) Aa	7.90 (2.21) Ca

Abbreviations: NPs: Undoped/unloaded nanoparticles; D-NPs; Doxycycline doped nanoparticles; Ca-NPs: Calcium doped nanoparticles; Zn-NPs: Zinc doped nanoparticles. Identical capital letter indicates no significant difference among distinct NPs at the same dentin half (cervical and apical) and storage period (24 h and 6 m). Identical lowercase means no significant difference among different dentin halves (cervical vs apical) at the same NPs group and storage period (24 h and 6 m). Asterisks mean significant difference between different storage periods (24 h *vs* 6 m) with the same NPs group at the same dentin half (cervical and apical).

Table S2. Data from Micro-X-ray diffraction pattern analysis of the different experimental groups.

			002 plane					310 plane					
	Disk	**Storage time**	**FWHM**	***H*: Scherrer equation (nm) (τ)**	**Scherrer-Wilson equation (nm)**	**Microstrain %**	**R_{hkl}**	**FWHM**	***L*: Scherrer equation (nm) (τ)**	**Scherrer-Wilson equation (nm)**	**Microstrain %**	**R_{hkl}**	***H/L***
AH Plus	Cervical	24h	0.0087	17.12	16.70	$1.8x10^{-6}$	0.561	0.0246	6.27	5.91	$1.8x10^{-5}$	1.152	2.73
		6m	0.0068	21.96	21.40	$1.1x10^{-6}$	0.561	0.0236	6.54	6.17	$1.3x10^{-5}$	1.221	3.36
	Apical	24h	0.0066	22.46	21.89	$1.1x10^{-6}$	0.463	0.0220	7.00	6.59	$1.1x10^{-5}$	1.230	3.21
		6m	0.0063	23.51	22.92	$9.8x10^{-7}$	0.430	0.0246	6.27	5.91	$1.4x10^{-5}$	1.234	3.75
NPs	Cervical	24h	0.0067	22.12	21.56	$1.1x10^{-6}$	0.461	0.0261	5.92	5.57	$1.6x10^{-5}$	1.230	3.74
		6m	0.0082	18.17	17.71	$1.6x10^{-6}$	0.501	0.0240	6.42	6.06	$1.4x10^{-5}$	1.176	2.83
	Apical	24h	0.0068	21.93	21.37	$1.1x10^{-6}$	0.428	0.0266	5.80	5.47	$1.7x10^{-5}$	1.232	3.78
		6m	0.0062	23.68	23.07	$9.6x10^{-7}$	0.470	0.0242	6.35	5.98	$1.4x10^{-5}$	1.231	3.73
D-NPs	Cervical	24h	0.0073	20.48	19.96	$1.3x10^{-6}$	0.469	0.0265	5.82	5.48	$1.7x10^{-5}$	1.210	3.52
		6m	0.0076	19.45	18.96	$1.4x10^{-6}$	0.495	0.0248	6.20	5.84	$1.5x10^{-5}$	1.218	3.13
	Apical	24h	0.0070	21.29	20.75	$1.1x10^{-6}$	0.514	0.0248	6.22	5.86	$1.4x10^{-5}$	1.239	3.42
		6m	0.0066	22.39	21.83	$1.1x10^{-6}$	0.485	0.0232	6.64	6.26	$1.3x10^{-5}$	1.334	3.37
Ca-NPs	Cervical	24h	0.0065	22.78	22.20	$1.0x10^{-6}$	0.452	0.0240	6.41	6.04	$1.4x10^{-5}$	1.308	3.55
		6m	0.0072	20.57	20.05	$1.3x10^{-6}$	0.461	0.0263	5.86	5.52	$1.6x10^{-5}$	1.163	3.51
	Apical	24h	0.0061	24.52	23.90	$9.0x10^{-7}$	0.404	0.0212	7.29	6.86	$1.1x10^{-5}$	1.358	3.36
		6m	0.0063	23.45	22.86	$9.8x10^{-7}$	0.454	0.0207	7.43	7.00	$1.0x10^{-5}$	1.325	3.16
Zn-NPs	Cervical	24h	0.0064	23.32	22.73	$9.9x10^{-7}$	0.419	0.0242	6.36	5.99	$1.4x10^{-5}$	1.246	3.67
		6m	0.0062	24.16	23.55	$9.2x10^{-7}$	0.400	0.0231	6.68	6.30	$1.2x10^{-5}$	1.396	3.61
	Apical	24h	0.0063	23.66	23.06	$9.6x10^{-7}$	0.477	0.02273	6.78	6.39	$1.2x10^{-5}$	1.339	3.49
		6m	0.0063	23.61	23.01	$9.7x10^{-7}$	0.471	0.02217	6.95	6.55	$1.2x10^{-5}$	1.240	3.40

Abbreviations: NPs: undoped/unloaded nanoparticles; D: Doxicicline; Ca: Calcium; Zn: Zinc; FWHM: Full-width half-maximum; R_{hkl}: texture.

Table S3. ANOVA results for microleakage, nanoindentation, Young's modulus, complex modulus, fiber diameter and nanoroughness.

	Microleakage	Young's modulus	Complex modulus	Fiber diameter	Nano-roughness
Multiple ANOVA	$p<0.01$	$p<0.03$	$p<0.03$	$p<0.03$	$p<0.02$
Nanoparticles (NPs)	$p<0.004$	$p<0.01$	$p<0.01$	$p<0.02$	$p<0.02$
Storage time	$p<0.005$	$p<0.02$	$p<0.03$	$p<0.05$	$p<0.05$
Dentin half (cervical-apical)	--	$p<0.05$	$p<0.05$	$p>0.05$	$p>0.05$
Dentin zone (peritubular-intratubular)	--	$p<0.04$	--	--	--
Interactions NPs-Storage time	$p<0.03$	$p<0.02$	$p<0.02$	$p<0.05$	$p<0.05$
Interactions NPs-Dentin half	--	$P<0.05$	$P<0.05$	$p>0.05$	$P<0.05$
Interactions NPs-Dentin zone	--	$P<0.05$	--	--	--
R^2 (model reliability)	0.83	0.70	0.69	0.59	0.71